Table 3 – Effects of TiO₂ on levels of chemokines in BALF and serum of RSV-infected mice on day 5 post-infection.[a]						
TiO₂ exposure (mg/kg)	Concentration in BALF (ng/mL)				Concentration in serum (ng/mL)	
	RSV-infected		Mock-infected		RSV-infected	Mock-infected
	CCL3	CCL5	CCL3	CCL5	CCL5	CCL5
0	0.10 ± 0.04	0.24 ± 0.06	<0.01	<0.01	0.14 ± 0.01	0.10 ± 0.01
0.5	0.11 ± 0.03	0.32 ± 0.07*	<0.01	<0.01	0.18 ± 0.03*	0.09 ± 0.03

[a] Concentration (ng/mL) of each chemokine in BALF and serum from RSV-infected mice treated with or without TiO₂ (0.5 mg/kg) was measured by ELISA for each specific chemokine. Data represents mean values of 3–6 mice. Numbers in parentheses indicate standard deviation.
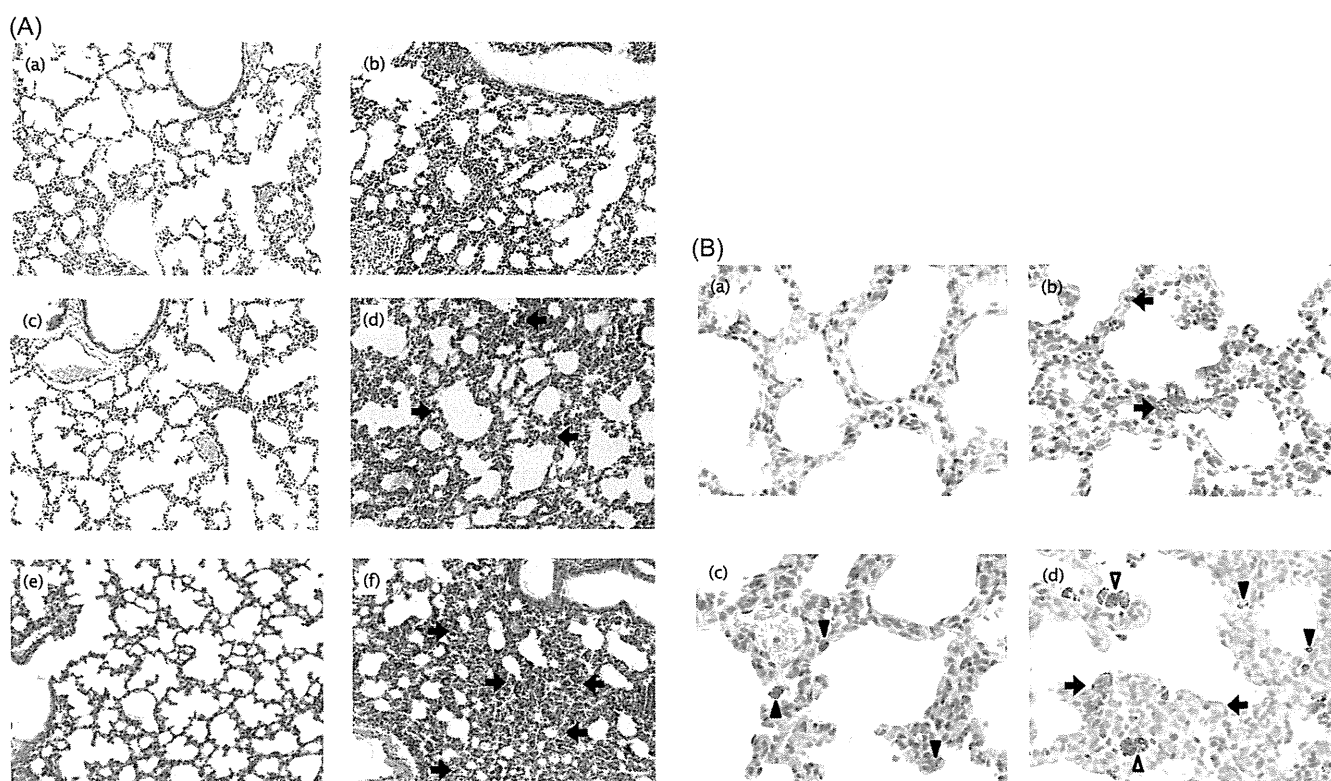* Statistically different from control at $P < 0.05$ (Student's t-test).

Fig. 2 – Lungs of mice 5 days after RSV-infection. (A) Hematoxylin and eosin staining (×100). (a) Control mouse with mock infection. (b) Control mouse with RSV infection. (c) TiO₂-treated (0.25 mg/kg) mouse with mock infection. (d) TiO₂-treated (0.25 mg/kg) mouse with RSV infection. (e) TiO₂-treated (2.5 mg/kg) mouse with mock infection. (f) TiO₂-treated (2.5 mg/kg) mouse with RSV infection. Arrows indicate infiltration of lymphocytes in alveolar septa. (B) Immunostained with anti-RSV protein antibodies (1:250) and counterstained with hematoxylin (×400). (a) Control mouse with mock infection. (b) Control mouse with RSV infection. (c) TiO₂-treated (2.5 mg/kg) mouse with mock infection. (d) TiO₂-treated (2.5 mg/kg) mouse with RSV infection. Closed arrows indicate RSV-positive cells, closed arrowheads indicate TiO₂ nanoparticles, and open arrowheads indicate aggregation of TiO₂ nanoparticles in inflammatory cells.

Table 4 – Effects of TiO₂ on proportion of tissue of alveolar septa in RSV-infected mice on day 5 post-infection.					
TiO₂ exposure (mg/kg)	% of alveolar tissues[a]				% of mean alveolar tissues
	>40	>50	>60	>70	
0	2*	2	0	0	51.8 (3.7)
0.25	0	2	2	0	60.6 (1.6)
2.5	0	0	1	1	68.6 (3.1)

[a] The proportion of tissue in alveolar septa per unit area by Adobe Photoshop.
* Number of mice. Numbers in parenthesis indicate the standard error.

Table 5 – Effects of TiO_2 on CCL3 production from bronchoalveolar lavage cells on day 1 post-infection in RSV-infected mice.

TiO_2 exposure (mg/mL)	CCL3 (ng/mL)[a]	
	−LPS	+LPS
0	<0.01	0.17 (0.12–0.23)*
0.1	<0.01	0.15 (0.13–0.16)

[a] Bronchoalveolar lavage cells were collected from RSV-infected mice and cultured for 48 h with or without TiO_2 (0.1 mg/mL).

* Data represent mean of values of two separate experiments. Numbers in parentheses indicate the range of values.

and 68.6% in each group, respectively. Thus, we confirmed exacerbation of the pneumonia due to RSV infection by TiO_2 exposure.

To investigate whether the distribution of RSV-infected cells was changed qualitatively due to TiO_2 (2.5 mg/kg) exposure, sections of the lung tissues of RSV-infected mice were stained immunohistochemically with a goat-polyclonal antibody against RSV protein (Fig. 2B). There was no significant change in the localization of RSV-positive cells, but the TiO_2 nanoparticles were not close to RSV-positive cells (Fig. 2B-b and -d). Similar results were observed for TiO_2 (0.25 mg/kg)-treated mice (data not shown). However, there was aggregation of TiO_2 nanoparticles near inflammatory cells in the severe region (Fig. 2B-d). Because these results suggested that TiO_2 nanoparticles might influence the function of macrophage/monocyte in an early phase of RSV infection, bronchoalveolar lavage cells on day 1 post-infection from RSV-infected mice were incubated for 48 h with or without 0.1 mg/mL of TiO_2, corresponding to a dose of 0.5 mg/kg *in vivo*. After incubation, the levels of CCL3 in the culture supernatant of the cells were measured by ELISA (Table 5). Although the cells were stimulated with LPS, there was no significant change in the production of CCL3 from bronchoalveolar lavage cells due to TiO_2 treatment.

4. Discussion

We assessed the effects of TiO_2 nanoparticles on the immune response using a mouse model of RSV infection (Watanabe et al., 2008a) and found that prior exposure to TiO_2 nanoparticles exacerbated pneumonia in the lungs of mice.

Various studies concerning risk assessment of TiO_2 nanoparticles in murine models have been reported (Chen et al., 2013; Kwon et al., 2012; Lindberg et al., 2012; Xu et al., 2010). In many cases, TiO_2 exposure was performed at a high dosage and/or multiple times. For example, to evaluate the carcinogenesis of TiO_2 nanoparticles in lung tissues, female (10 weeks old) SD rats were subjected to intra-pulmonary spraying five times with 0.5 mL suspensions of TiO_2 nanoparticles at 500 μg/mL in saline (Xu et al., 2010). In our assay, female (6 weeks old) BALB/c mice were exposed once intranasally to 0.1 mL of a suspension of TiO_2 nanoparticles at 50 μg/mL or 100 μg/mL, corresponding to a dose of 0.25 mg/kg or 0.5 mg/kg of body weight. The levels of TiO_2 exposure in our assay are much lower than those in previous studies (Chen et al., 2013; Kwon et al., 2012; Lindberg et al., 2012; Xu et al., 2010), and

suppression of body weight, abnormal behavior, or dystrophy due to the stress of TiO_2 exposure was not observed compared with the control mice (data not shown). Furthermore, in the TiO_2-treated mice without RSV infection, no significant enhancement of cytokines or chemokines in BALF and any obvious changes in lung tissues were observed (Table 1, 3, Fig. 2A-a, -c, -e, B-a, and -c). Based on these experiments, we are confident that RSV infection is a useful tool for evaluation of the effects of low-level exposure to TiO_2 nanoparticles on the immune system, which was not reported previously.

The IFN-γ levels of RSV-infected mice treated with TiO_2 were enhanced significantly ($P < 0.05$) compared with the control (Table 1). These results suggest that pneumonia in RSV-infected mice was exacerbated due to TiO_2 exposure. However, viral titers in lung tissues of RSV-infected mice exposed to TiO_2 were not elevated significantly compared with the control (Fig. 1), and there was no significant increase of the number of RSV-positive cells in lung tissues due to TiO_2 exposure (Fig. 2B). Previous studies concerning evaluation of immunotoxicity of BFRs such as DBDE and TBBPA have shown that these compounds clearly increased both the levels of IFN-γ and viral titers in RSV-infected mice, resulting in the exacerbation of pneumonia (Watanabe et al., 2008b, 2010a,b). Therefore, we speculated that the mechanism of action of TiO_2 nanoparticles was different from that of BFRs on the immune system (Watanabe et al., 2008b, 2010a,b). We investigated further effects of exposure to TiO_2 on the Th1/2 balance of RSV-infected mice. The levels of IL-10, a Th2 cytokine, in BALF were increased significantly ($P < 0.05$) compared with the control (Table 1). IL-10 is produced mainly by T cells and acts by inhibiting the production of pro-inflammatory cytokines (Cavalcanti et al., 2012). Remarkably, although enhancement of the IL-10 levels should alleviate immune response, exacerbation of pneumonia was conversely exhibited (Fig. 2A). On the other hand, enhancement of IL-4 production due to TiO_2 exposure was not observed (Table 1). However, the levels of chemokine CCL5, an inflammatory marker called RANTES produced mainly by T cells and basophils (Schall et al., 1988), in BALF were also increased significantly ($P < 0.05$) compared with the control (Table 3). Thus, this irregular activation of T cells due to TiO_2 exposure might induce a Th1/2 imbalance. However, there was not a significant change in the population of IFN-γ-positive cells and IL-4-positive cells due to TiO_2 treatment by flow cytometric analysis (Table 2). These results suggested that TiO_2 exposure probably affected the secretion of the cytokines rather than differentiation of $CD4^+$ cells, responding to RSV infection.

In the histopathological analysis, the infiltration of lymphocytes in alveolar septa in RSV-infected mice tended to be increased by TiO_2 exposure, particularly in wide areas of lung tissues (Fig. 2A and Table 4). Because chemokine CCL5 promotes the migration of T cells and basophils (Schall et al., 1988), enhancement of it should contribute to the infiltration (Table 3). Moreover, in an immunohistochemical analysis, we observed TiO_2 nanoparticles explicitly because the sections were faintly counterstained with hematoxylin (Fig. 2B). It became evident that TiO_2 nanoparticles were aggregated by lymphocytes/macrophages but were not close to RSV-positive cells. It has been reported that TiO_2 nanoparticles were engulfed in alveolar macrophages and involved in the

inflammation in lung tissues of the TiO_2-treated rodents (Kwon et al., 2012; Xu et al., 2010). Then, to evaluate whether TiO_2 exposure influence the function of macrophages/monocytes in lung tissue of RSV-infected mice, the bronchoalveolar lavage cells on day 1 post-infection, consist mainly of the macrophage/monocyte-like cells (Watanabe et al., 2010a), were cultured with or without TiO_2 (Table 5). The *in vitro* experiment using a LPS showed that TiO_2 treatment did not affect the production of chemokine CCL3 from the bronchoalveolar lavage cells, although the ingestion of TiO_2 nanoparticles in the macrophage/monocyte-like cells was observed under a microscope. Therefore, further studies are needed to understand whether macrophages are involved in the immune response in an early phase of RSV infection.

TiO_2 nanoparticles are used in various products, and we may be exposed to them at various times of life. We have already confirmed that anatase crystals of TiO_2 nanoparticles used in building materials induced the elevation of CCL5 in RSV-infected mice (data not shown). In this study, we used TiO_2 nanoparticles that form rutile crystals and are used in cosmetics. Further studies are required to investigate the effects of TiO_2 nanoparticles of different forms and sizes on immune response. These studies should provide useful information to manage their effects on health, including methods of skin care.

Conflict of interests

The authors declare that they have no conflict of interests.

Acknowledgments

REFERENCES

Cavalcanti, Y.V., Brelaz, M.C., Neves, J.K., Ferraz, J.C., Pereira, V.R., 2012. Role of TNF-alpha, IFN-gamma, and IL-10 in the development of pulmonary tuberculosis. Pulm. Med. 2012, 745483.

Chen, T., Hu, J., Chen, C., Pu, J., Cui, X., Jia, G., 2013. Cardiovascular effects of pulmonary exposure to titanium dioxide nanoparticles in ApoE knockout mice. J. Nanosci. Nanotechnol. 13, 3214–3222.

Collins, P.L., Chanock, R.M., Murphy, B.R., 2001. Respiratory syncytial virus. In: Knipe, D.M., Howley, P.M. (Eds.), Fields Virology. Lippincott Willams & Wilkins, Philadelphia, PA, pp. 1443–1485.

Falsey, A.R., 2007. Respiratory syncytial virus infection in adults. Semin. Respir. Crit. Care Med. 28, 171–181.

Falsey, A.R., Hennessey, P.A., Formica, M.A., Cox, C., Walsh, E.E., 2005. Respiratory syncytial virus infection in elderly and high-risk adults. N. Engl. J. Med. 352, 1749–1759.

Holberg, C.J., Wright, A.L., Martinez, F.D., Ray, C.G., Taussig, L.M., Lebowitz, M.D., 1991. Risk factors respiratory syncytial virus-associates lower respiratory illnesses in the first year of life. Am. J. Epidemiol. 133, 1135–1151.

Huerta-Garcia, E., Pérez-Arizti, J.A., Márquez-Ramírez, S.G., Delgado-Buenrostro, N.L., Chirino, Y.I., Iglesias, G.G., López-Marure, R., 2014. Titanium dioxide nanoparticles induce strong oxidative stress and mitochondrial damage in glial cells. Free Radic. Biol. Med. 73, 84–94.

Kwon, S., Yang, Y.S., Yang, H.S., Lee, J., Kang, M.S., Lee, B.S., Lee, K., Song, C.W., 2012. Nasal and pulmonary toxicity of titanium dioxide nanoparticles in rats. Toxicol. Res. 28, 217–224.

Lambert, A.L., Trasti, F.S., Mangum, J.B., Everitt, J.I., 2003. Effects of preexposure to ultrafine carbon black on respiratory syncytial virus infection in mice. Toxicol. Sci. 72, 331–338.

Lindberg, H.K., Flack, G.C., Catalán, J., Koivisto, A.J., Suhonen, S., Järventaus, H., Rossi, E.M., Nykäsenoja, H., Peltonen, Y., Moreno, C., Alenius, H., Tuomi, T., Savolainen, K.M., Norppa, H., 2012. Genotoxicity of inhales nanosized TiO(2) in mice. Mutat. Res. 745, 58–64.

MacDonald, N.E., Hall, C.B., Suffin, S.C., Alexson, C., Harris, P.J., Manning, J.A., 1982. Respiratory syncytial viral infection in infants with congenital heart disease. N. Engl. J. Med. 307, 397–400.

Maidalawieh, A., Kanan, M.C., E.I-Kadri, O., Kanan, S.M., 2014. Recent advances in gold and silver nanoparticles: synthesis and applications. J. Nanosci. Nanotechnol. 14, 4547–4580.

Nel, A., Xia, T., Mädler, L., Li, N., 2006. Toxic potential of materials at the nanolevel. Science 311, 622–627.

Schall, T.J., Jongstra, J., Dyer, B.J., Jorgensen, J., Clayberger, C., Davis, M.N., Krensky, A.M., 1988. A human T cell-specific molecule is a member of a new gene family. J. Immunol. 141, 1018–1025.

Stamatoiu, O., Mirzaei, J., Feng, X., Hegmann, T., 2012. Nanoparticles in liquid crystals and liquid crystalline nanoparticles. Top. Curr. Chem. 318, 331–393.

Takeda, S., Hidaka, M., Yoshida, H., Takeshita, M., Kikuchi, Y., Tsend-Ayush, C., Dashnyam, B., Kawahara, S., Muguruma, M., Watanabe, W., Kurokawa, M., 2014. Antiallergic activity of probiotics from Mongolian dairy products on type I allergy in mice and mode of antiallergic action. J. Funct. Foods 9, 60–69.

Takeshita, T., Watanabe, W., Toyama, S., Hayashi, Y., Honda, S., Sakamoto, S., Matsuoka, S., Yoshida, H., Takeda, S., Hidaka, M., Tsutsumi, S., Yasukawa, K., Park, Y.K., Kurokawa, M., 2013. Effects of Brazilian propolis on exacerbation of respiratory syncytial virus infection in mice exposed to tetrabromobisphenol a, a brominated flame retardant. Evid. Based Complement. Altern. Med. 2013, 698206.

Watanabe, W., Shimizu, T., Hino, A., Kurokawa, M., 2008a. A new assay system for evaluation of developmental immunotoxicity of chemical compounds using respiratory syncytial virus infection to offspring mice. Environ. Toxicol. Pharmacol. 25, 69–74.

Watanabe, W., Shimizu, T., Hino, A., Kurokawa, M., 2008b. Effects of decabrominated diphenyl ether (DBDE) on developmental immunotoxicity in offspring mice. Environ. Toxicol. Pharmacol. 26, 315–319.

Watanabe, W., Shimizu, T., Sawamura, R., Hino, A., Konno, K., Kurokawa, M., 2010a. Functional disorder of primary immunity responding to respiratory syncytial virus infection in offspring mice exposed to a flame retardant, decabrominated dephenyl ether, perinatally. J. Med. Virol. 82, 1075–1082.

Watanabe, W., Shimizu, T., Sawamura, R., Hino, A., Konno, K., Hirose, A., Kurokawa, M., 2010b. Effects of tetrabromobisphenol A, a brominated flame retardant, on the immune response to respiratory syncytial virus infection in mice. Int. Immunopharmacol. 10, 393–397.

Watanabe, W., Yoshida, H., Hirose, A., Akashi, T., Takeshita, T., Kuroki, N., Shibata, A., Hongo, S., Hashiguchi, S., Konno, K., Kurokawa, M., 2013. Perinatal exposure to insecticide methamidophos suppressed production of proinflammatory cytokines responding to virus infection in lung tissues in mice. Biomed. Res. Int., 151807.

Xu, J., Futakuchi, M., Iigo, M., Fukamachi, K., Alexander, D.B., Shimizu, H., Sakai, Y., Furukawa, F., Uchino, T., Tokunaga, H., Nishimura, T., Hirose, A., Kanno, J., Tsuda, H., 2010.

Involvement of macrophage inflammatory protein 1 alpha (MIP1alpha) in promotion of rat lung and mammary carcinogenic activity of nanoscale titanium dioxide particles administered by intra-pulmonary spraying. Carcinogenesis 31, 927–935.

Zhang, H., Wang, C., Chen, B., Wang, X., 2012. Daunorubicin-TiO_2 nanocomposites as a smart pH-responsive drug delivery system. Int. J. Nanomed. 7, 235–242.

Cancer Science

Size- and shape-dependent pleural translocation, deposition, fibrogenesis, and mesothelial proliferation by multiwalled carbon nanotubes

Jiegou Xu,[1,2] David B. Alexander,[1] Mitsuru Futakuchi,[3] Takamasa Numano,[3] Katsumi Fukamachi,[3] Masumi Suzui,[3] Toyonori Omori,[4] Jun Kanno,[5] Akihiko Hirose[6] and Hiroyuki Tsuda[1]

[1]Laboratory of Nanotoxicology Project, Nagoya City University, Nagoya, Japan; [2]Department of Immunology, Anhui Medical University College of Basic Medical Sciences, Hefei, China; [3]Department of Molecular Toxicology, Nagoya City University Graduate School of Medical Sciences, Nagoya; [4]Air Environment Division Environment Management Bureau, Ministry of the Environment, Government of Japan, Tokyo; [5] Divisions of Cellular and Molecular Toxicology; [6] Risk Assessment, National Institute of Health Sciences, Tokyo, Japan

Multiwalled carbon nanotubes (MWCNT) have a fibrous structure similar to asbestos, raising concern that MWCNT exposure may lead to asbestos-like diseases. Previously we showed that MWCNT translocated from the lung alveoli into the pleural cavity and caused mesothelial proliferation and fibrosis in the visceral pleura. Multiwalled carbon nanotubes were not found in the parietal pleura, the initial site of development of asbestos-caused pleural diseases in humans, probably due to the short exposure period of the study. In the present study, we extended the exposure period to 24 weeks to determine whether the size and shape of MWCNT impact on deposition and lesion development in the pleura and lung. Two different MWCNTs were chosen for this study: a larger sized needle-like MWCNT (MWCNT-L; l = 8 μm, d = 150 nm), and a smaller sized MWCNT (MWCNT-S; l = 3 μm, d = 15 nm), which forms cotton candy-like aggregates. Both MWCNT-L and MWCNT-S suspensions were administered to the rat lung once every 2 weeks for 24 weeks by transtracheal intrapulmonary spraying. It was found that MWCNT-L, but not MWCNT-S, translocated into the pleural cavity, deposited in the parietal pleura, and induced fibrosis and patchy parietal mesothelial proliferation lesions. In addition, MWCNT-L induced stronger inflammatory reactions including increased inflammatory cell number and cytokine/chemokine levels in the pleural cavity lavage than MWCNT-S. In contrast, MWCNT-S induced stronger inflammation and higher 8-hydroxydeoxyguanosine level in the lung tissue than MWCNT-L. These results suggest that MWCNT-L has higher risk of causing asbestos-like pleural lesions relevant to mesothelioma development.

P leural plaque and malignant mesothelioma are characteristic lesions in asbestos-exposed humans and usually originate from the parietal pleura.[1,2] Properties of asbestos fibers, including dimension, chemical composition, surface reactivity, durability and biopersistence, asbestos deposition-induced oxidative stress and inflammation, and simian virus 40 infection have all been implicated in the pathogenesis of pleural diseases, especially malignant mesothelioma.[3,4]

High concentrations of asbestos fibers have been found in the black spots of the parietal pleura[5] and detected in pleural plaques and malignant mesothelioma[6] in asbestos-exposed patients, suggesting that deposition of asbestos fibers in the parietal pleura is an early event and plays an important role in the pathogenesis of pleural lesions. However, why parietal pleura are the initial and preferential targets of asbestos is not known. According to an explanatory paradigm suggested by Donaldson *et al.*,[7] a fraction of the fibers in the lung are routinely transported into the pleural cavity through unidentified routes. Unlike spherical particles and short fibers, long fibers cannot be cleared effectively through the stomata (small holes

in the parietal pleura), resulting in the long fibers being trapped and deposited in the parietal pleura. This deposition causes pro-inflammatory, genotoxic, and mitogenic responses in the deposition sites.[7]

Carbon nanotubes have a fibrous structure with a high aspect ratio. This structural feature, shared with asbestos, raises concern that widespread use of carbon nanotubes may lead to asbestos-like diseases in exposed humans.[8,9] Multiwalled carbon nanotubes (MWCNT) directly injected into the peritoneal cavity or the scrotum in rodents induce mesothelial lesions, including malignant mesothelioma,[10–13] suggesting that inhaled MWCNT may lead to pleural plaque and mesothelioma if fibers enter the pleural cavity. Furthermore, MWCNT administered to the lung has been found to translocate into the pleural cavity and induce inflammation in the pleural cavity and mesothelial cell proliferation in the visceral pleura in mice and rats.[14–16] However, deposition of MWCNT and induction of associated lesions in the parietal pleura have not been reported.

The pleural responses to fibrous particles that deposit in the pleural cavity depend on the size of the particle. Murphy

et al.[17] reported that intrapleural injection of long (>15 μm) but not short (<4 μm) MWCNT caused persistent inflammation and fibrosis of the parietal pleura up to 24 weeks post-treatment. Similarly, Schinwald et al.[18] reported that injection of silver nanofibers with different lengths into the pleural cavity showed a clear length threshold effect, indicating that fibers longer than 4 μm were pathogenic to the pleura.

The main purpose of the present study was to determine if the size and shape of inhaled MWCNT impact on deposition and associated lesion development in the parietal and visceral pleura. Two different MWCNT were chosen for this study: larger needle-like MWCNTs (MWCNT-L, $l = 8$ μm, $d = 150$ nm) and smaller-sized MWCNT (MWCNT-S, $l = 3$ μm, $d = 15$ nm) that form cotton candy-like aggregates. We gave relatively high doses (125 μg/rat × 13 doses) of the two MWCNT suspensions over a 24-week period to the rat lung by transtracheal intrapulmonary spraying (TIPS) in order to examine detectable fibers and associated inflammatory and proliferative lesions in the pleura.

Materials and Methods

Animals. Eight-week-old male F344 rats (Charles River, Kanagawa, Japan) were housed on a 12:12 h light:dark cycle and received Oriental MF basal diet (Oriental Yeast, Tokyo, Japan) and water ad libitum. The study was conducted according to the Guidelines for the Care and Use of Laboratory Animals of Nagoya City University Medical School (Nagoya, Japan) and the experimental protocol was approved by the Institutional Animal Care and Use Committee (H22M-19).

Preparation of MWCNT suspensions. We used two types of MWCNTs grown in the vapor phase. The larger-sized MWCNTs (MWCNT-L) had a primary mean length of 8 μm and a diameter of 150 nm, and the smaller-sized MWCNTs (MWCNT-S) had a primary mean length of 3 μm and a diameter of 15 nm. Five milligrams of MWCNT-L or MWCNT-S were suspended in 20 mL saline containing 0.5% Pluronic F68 (PF68, non-ionic, biocompatible amphiphilic block copolymers; Sigma-Aldrich, St. Louis, MO, USA) and homogenized for 1 min four times at 3000 rpm in a Polytron PT1600E benchtop homogenizer (Kinematika, Littau, Switzerland). The suspensions were sonicated for 30 min shortly before use to minimize aggregation. The concentration of MWCNTs was 250 μg/mL. The lengths of MWCNT-L in the suspensions were determined using a digital map meter (Comcurve-9 Junior; Koizumi Sokki, Nigata, Japan) on SEM photographs. Characterization of MWCNT including shape, elemental analysis, and size distribution is shown in Figure S1.

Transtracheal intrapulmonary spraying of MWCNTs into the lung and pleural cavity lavage. Spraying of MWCNT suspensions into the lung and pleural cavity lavage (PCL) were carried out as previously described.[15,19] Ten-week-old male Fisher 344 rats were divided into four groups of six animals each. Group 1 did not receive any treatment, and Groups 2, 3, and 4 were given 0.5 mL saline containing 0.5% PF68 or 250 μg/mL MWCNT-L or MWCNT-S suspensions by TIPS under anesthesia by isoflurane once every 2 weeks, 13 times over a 24-week period. The total amount of the MWCNT fibers given to Groups 3 and 4 was 13 × 0.125 = 1.625 mg/rat. Twenty-four hours after the last TIPS, the rats were placed under deep isoflurane anesthesia and PCL was carried out. The rats were then killed by exsanguination from the inferior vena cava. The left lung was frozen in liquid nitrogen for biochemi-

cal analysis, and the right lung, as well as other major organs and lymph nodes, were processed for histological examination.

Light microscopy, polarized light microscopy, and SEM. The MWCNT fibers in H&E stained slides of lung tissue, PCL cell pellets, and chest wall sections were observed with polarized light microscopy (PLM, BX51N-31P-O; Olympus, Tokyo, Japan) at ×1000 magnification. The exact localization of the illuminated fibers was confirmed in the same H&E stained sections after removing the polarizing filter.

For SEM, H&E stained slides were immersed in xylene for 2–3 days to remove the cover glass, immersed in 100% ethanol for 10 min to remove the xylene, and air-dried for 2 h at room temperature. The slides were then coated with platinum for viewing the MWCNT fibers by SEM (Model S-4700 Field Emission Scanning Electronic Microscope; Hitachi High Technologies, Tokyo, Japan) at 5–10 kV.

Azan–Mallory staining and measurement of the thickness of the parietal and visceral pleura. To clearly visualize collagen fibers in the lung and the pleura, Azan–Mallory staining was carried out using Azan staining reagents (Muto Pure Chemicals, Tokyo, Japan). The thickness of the pleura was measured on the basis of the Azan–Mallory stained sections (Fig. S2). For the rats treated with MWCNT-L, only the parietal and visceral pleural regions with observed MWCNT-L fibers by PLM were measured. Because obvious thickening of the pleura was not observed in the rats treated with PF68 or MWCNT-S, six pleural regions in each parietal and visceral pleura of each rat were randomly selected for measurement.

Analysis of inflammatory reaction in the pleural cavity. Cells in the lavage fluid were counted using a hemocytometer (Erma, Tokyo, Japan), and the cellular fraction was then isolated by centrifugation at 200g for 5 min at 4°C. To make cell pellets, cells collected from three rats were combined (generating a total of two cell pellets per group) and resuspended in 0.2 mL of 1% sodium alginate (Sigma-Aldrich) by pipetting. The suspension was then solidified by addition of one drop of 1 M CaCl₂. The cell pellets were fixed in 4% paraformaldehyde and processed for histological examination. Total protein in the supernatants of each of the lavage fluids was determined using the Pierce BCA Protein Assay Kit (Thermo Fisher Scientific, Rockford, IL, USA). Cytokines and chemokines were analyzed as described below.

Analysis of cytokines and chemokines by Multiplex Suspension Array. Approximately 100 mg of the left lung tissues was rinsed with cold PBS three times and homogenized in 1 mL T-PER Tissue Protein Extraction Reagent (Pierce, Rockford, IL, USA), containing 1% (v/v) proteinase inhibitor cocktail (Sigma-Aldrich). The homogenates were clarified by centrifugation at 10 000 g for 5 min at 4°C. Protein content was measured as described above. The levels of 20 cytokines and chemokines (interleukin [IL]-1α, IL-1β, IL-2, IL-4, IL-6, IL-12 [p70], IL-17, IL-18, granulocyte/macrophage colony-stimulating factors [GM-CSF], granulocyte colony-stimulating factor [G-CSF], tumor necrosis factor [TNF]-α, γ-interferon, monocyte chemotactic protein [MCP]1, macrophage inflammatory protein [MIP]1α, MIP2, interferon gamma-induced protein [IP]-10, regulated on activation, normal T cell expressed and secreted [RANTES], growth related oncogene/ keratinocyte-derived cytokine [GRO/KC], vascular endothelial growth factor [VEGF], and epidermal growth factor [EGF]) in the lung tissue extracts and in the supernatants of the lavage fluids were measured by the Multiplex MAP Rat Cytokine/Chemokines Magnetic Bead Panel (Filgen, Nagoya, Japan).

Immunohistochemistry. CD68, proliferating cell nuclear antigen (PCNA), and mesothelin/Erc were detected using anti-rat CD68 antibodies (BMA Biomedicals, Augst, Switzerland), anti-

PCNA mAbs (Clone PC10; Dako Japan, Tokyo, Japan) and anti-rat C-ERC/mesothelin polyclonal antibodies (Immuno-Biological Laboratories, Gunma, Japan). The CD68, PCNA, and C-ERC/mesothelin antibodies were diluted 1:100, 1:200, and 1:1000, respectively, in blocking solution and applied to deparaffinized slides, and the slides were incubated at 4°C overnight. The slides were then incubated for 1 h with biotinylated species-specific secondary antibodies diluted 1:500 (Vector Laboratories, Burlingame, CA, USA) and visualized using avidin-conjugated HRP complex (ABC kit; Vector Laboratories).

Statistical analysis. Statistical analysis was carried out using ANOVA. Statistical significance was analyzed using two-tailed Student's t-test. A P-value of <0.05 was considered to be significant.

Results

Deposition of MWCNT-L in the pleura. Observation of the pleural tissue sections with PLM and SEM indicated that MWCNT-L deposited in the parietal pleura in four out of six rats, most of the fibers being located in fibrotic parietal pleura, with a few piercing and penetrating into the parietal mesothelium (Fig. 1a–c); MWCNT-L was also found in the visceral pleura (Fig. 1d–f).

Smaller sized MWCNT did not cause polarization and consequently were not detected by PLM (Fig. 1h,k); therefore, observation of MWCNT-S was made mainly by SEM. The MWCNT-S were not found in either the parietal (Fig. 1g–i) or visceral (Fig. 1j) pleura and were often found phagocytosed in alveolar macrophages close to the visceral pleura (Fig. 1j–l).

Fibrosis and mesothelial proliferation in the pleura. Deposition of MWCNT-L in the parietal and visceral pleura was preferentially localized in thickened fibrotic lesions (Fig. 1a,d). Azan–Mallory staining indicated that the thickened lesions were composed of collagen fibers (Fig. 2a). The thickness of the parietal and visceral pleura with deposition of MWCNT-L was 28.75 ± 10.43 µm and 18.92 ± 10.13 µm, respectively, both lesions showing a significant increase compared to those in the rats treated with MWCNT-S (7.28 ± 4.37 µm and 6.16 ± 2.05 µm) or with the dispersing agent, PF68, alone (7.16 ± 4.95 µm and 4.57 ± 1.23 µm; Fig. 2b). An increase in the thickness of the visceral pleura of the rats treated with MWCNT-S compared with the PF68-treated rats was also observed (Fig. 2b).

Neoplastic development was not found in the parietal or visceral pleura of either the MWCNT-L or MWCNT-S groups; however, in the MWCNT-L group, patchy foci of mesothelial cell proliferation were observed in the parietal pleura (Fig. 3a) and PCNA indices were significantly increased in both parietal and visceral mesothelium. The PCNA indices of the MWCNT-S group were comparable to those of the PF68 treated rats (Fig. 3b).

Translocation of MWCNT-L into the pleural cavity. In the cell pellets of the PCL, MWCNT-L was found with both PLM and SEM observations. Larger sized MWCNT fibers were observed mainly within and/or attached to the cell surface of macrophages (Fig. 4a). The ratio of the MWCNT-L containing macrophages to the total cell count was approximately 1:1800 and the average length of MWCNT-L was 6.23 ± 4.11 µm (data not shown). Smaller sized MWCNT could not be detected (Fig. 4a).

Inflammation in the pleural cavity. Both MWCNT-L and MWCNT-S treatments caused inflammatory reactions in the
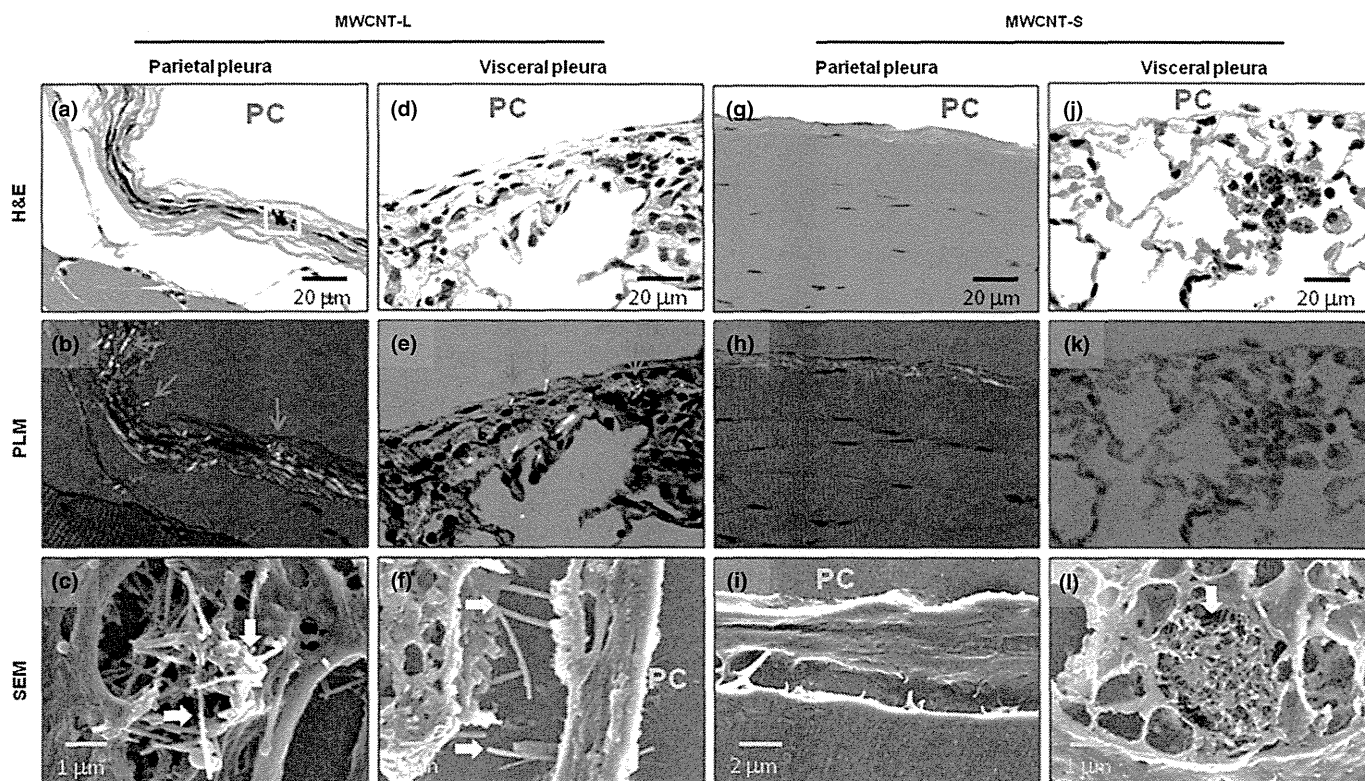

Fig. 1. Evidence of multiwalled carbon nanotube (MWCNT) fibers in the pleura. Existence of MWCNT fibers in the parietal (a–c, g–i) and visceral (d–f, j–l) pleura of rats treated with larger sized MWCNT (MWCNT-L; l = 8 µm, d = 150 nm) (a–f) or smaller sized MWCNT (MWCNT-S; l = 3 µm, d = 15 nm) (g–l) was examined by polarized light microscopy (PLM) (d, e, h, k) and SEM (c, f, i, l). The area in (a) denoted by the square was subjected to SEM observation, shown in (c). Arrows indicate MWCNT fibers. PC, pleural cavity.
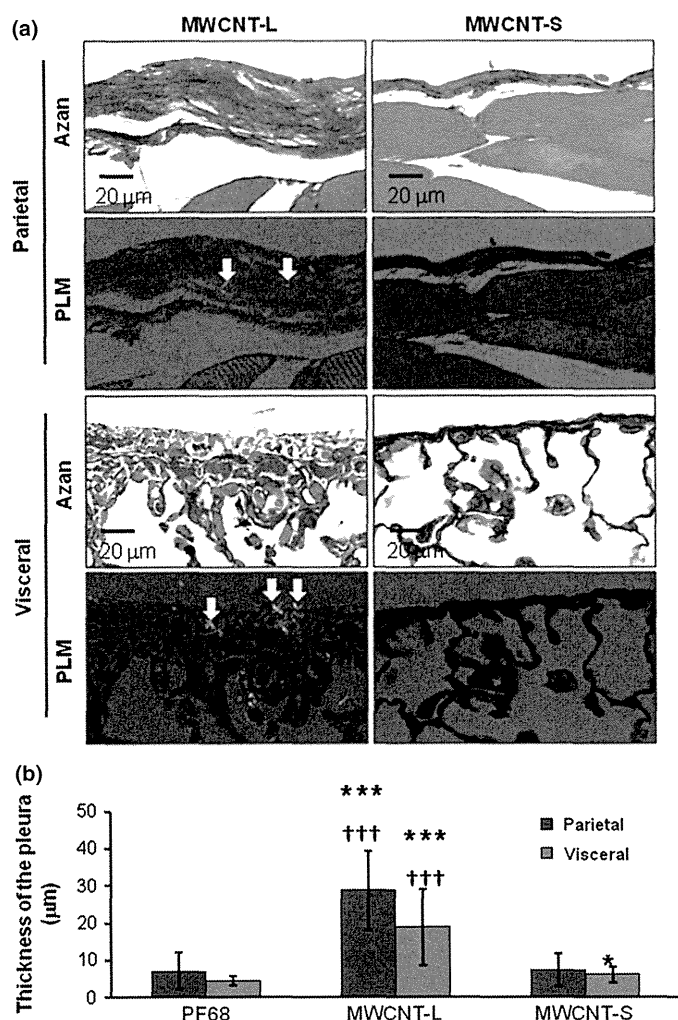
Fig. 2. Azan–Mallory (Azan) staining and thickness of the parietal and visceral pleura. (a) Azan–Mallory staining images and polarized light microscopy (PLM) images of the parietal and visceral pleura in rats sprayed with larger sized multiwalled carbon nanotubes (MWCNT-L; l = 8 μm, d = 150 nm) or smaller sized MWCNT (MWCNT-S; l = 3 μm, d = 15 nm). (b) Quantification of the thickness of the parietal and visceral pleura of rats treated with Pluronic F68 (PF68), MWCNT-L, or MWCNT-S on the basis of Azan–Mallory stained images. *P < 0.05 versus PF68; ***P < 0.001 versus PF68; †††P < 0.001 MWCNT-L versus MWCNT-S by two-tailed Student's t-test. Arrows indicate MWCNT fibers.

Fig. 3. Cell proliferation of the parietal and visceral mesothelium. (a) Representative proliferating cell nuclear antigen (PCNA) immunostained images of the parietal and visceral pleural regions of rats treated with larger sized multiwalled carbon nanotubes (MWCNT-L; l = 8 μm, d = 150 nm) or smaller sized MWCNT (MWCNT-S; l = 3 μm, d = 15 nm). (b) PCNA indices (percentages of PCNA positive mesothelial cells in total mesothelial cells). Scale bar = 20 μm. **P < 0.01 versus Pluronic F68 (PF68); ††P < 0.01 MWCNT-L versus MWCNT-S.

pleural cavity. In the PCL, the total cell number, composed mostly of macrophages, neutrophils, eosinophils, and lymphocytes, in the MWCNT-L and MWCNT-S treated groups was significantly increased compared with the PF68 group. The PCL cell number in the MWCNT-L group was significantly greater than in the MWCNT-S group (Fig. 4b). A similar pattern was observed for the ratio of cells positive for CD-68, a macrophage/monocyte marker (Fig. 4c). The ratios of cells in the PCL pellets positive for mesothelin/Erc, a mesothelial cell marker, were approximately 1%, indicating that the increased cell number in the pleural cavity of the rats treated with MWCNT-L and MWCNT-S was caused by inflammatory cell effusion, not by mesothelial cell shedding from the mesothelium. Treatment with MWCNT-L also caused an increase in the total protein level of the cell-free PCL (Fig. 4d). Analysis
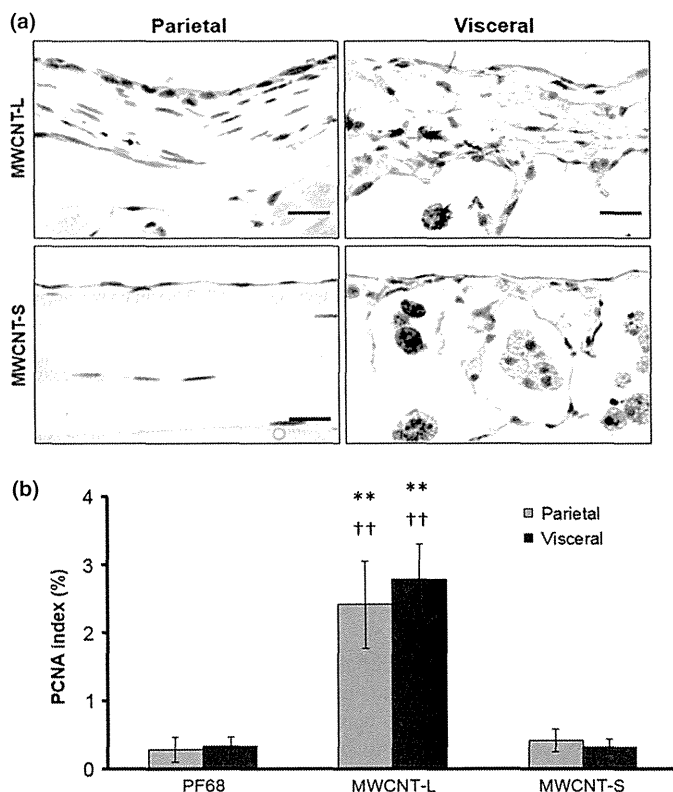
of 20 cytokines and chemokines by Multiplex Suspension Array indicated that the levels of IP-10, RANTES, IL-2, and IL-18 were significantly higher in the MWCNT-L group than the MWCNT-S group (Table 1).

Toxicological responses in the lung. In the lung tissue, both MWCNT-L and MWCNT-S treatments induced small granulation foci and scattered infiltration of macrophages in the alveoli (Fig. S3A,B). Alveolar neoplastic proliferation was not found. The number of alveolar macrophages was higher in the MWCNT-S group than in the MWCNT-L group. We were unable to quantitatively analyze the alveolar macrophage number, because most of the alveolar macrophages induced by MWCNT-S were degenerative or necrotic. Most of the MWCNT-L fibers were found within alveolar macrophages (Fig. S3C), with a few penetrating the alveolar epithelium (Fig. S3D), whereas MWCNT-S fibers were observed in alveolar macrophages, but not in the alveolar epithelium (Fig. S3E). Multiplex Suspension Array analysis of 20 cytokines and chemokines in the lung tissue indicated that the levels of MIP1α, MIP2, MCP1, IP10, IL-1β, IL-18, and VEGF were significantly higher in the MWCNT-S group than in the MWCNT-L group; the values of GRO/KC and IL-1α were elevated in both the MWCNT-L and MWCNT-S treated groups without an intergroup difference. The level of RANTES was significantly higher in the MWCNT-L group than the MWCNT-S group, and the other 10 cytokines were compara-
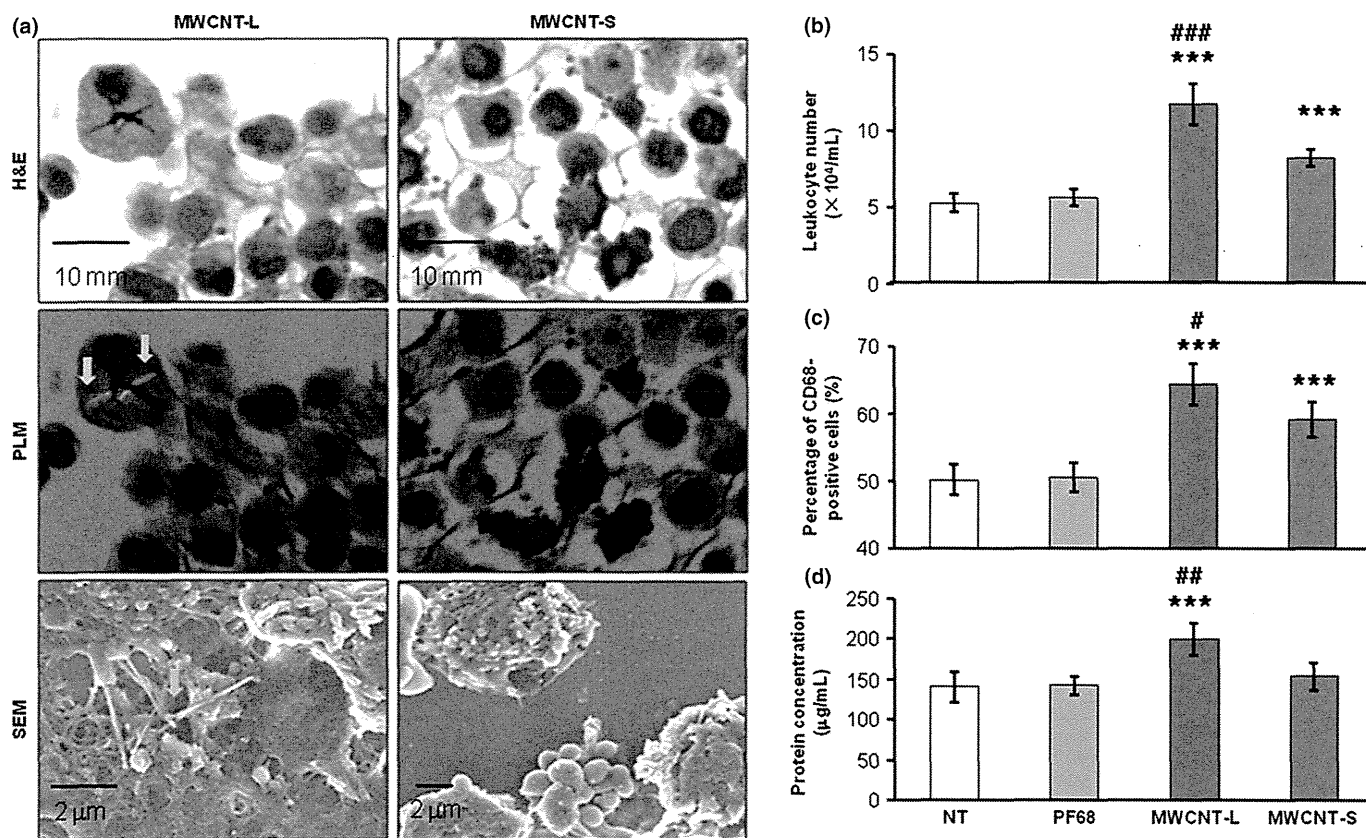
Fig. 4. Demonstration of multiwalled carbon nanotube (MWCNT) fibers and analysis of inflammatory reactions in the pleural cavity. (a) H&E staining, polarized light microscopy (PLM), and SEM images of pleural cell pellets taken from rats treated with larger sized MWCNT (MWCNT-L; l = 8 μm, d = 150 nm) or smaller sized MWCNT (MWCNT-S; l = 3 μm, d = 15 nm). Arrows indicate MWCNT fibers. (b–d) Analysis of leukocyte number (b), proportion of CD 68-positive cells (c), and protein concentration (d) in the supernatants of pleural cavity lavages. ***P < 0.001 versus Pluronic F68 (PF68); #P < 0.05, ##P < 0.01, and ###P < 0.001 MWCNT-L versus MWCNT-S by two-tailed Student's t-test. NT, no treatment.

ble among the PF68, MWCNT-L, and MWCNT-S treated groups (Table 1). Smaller sized MWCNT were more potent than MWCNT-L in inducing 8-hydroxydeoxyguanosine (8-OHdG), a marker for oxidative stress, in the lung tissue (Fig. S3F).

Transportation of MWCNT-L to extrapulmonary organs. In addition to the lung and pleura, MWCNT-L was found in extrapulmonary organs. Polarized light microscopy observations indicated that MWCNT-L was transported to the mediastinal (Fig. S4A), submandibular (Fig. S4B), and mesentery (Fig. S4C) lymph nodes, with many more fibers in the mediastinal lymph nodes than in the other examined lymph nodes. A few MWCNT-L fibers were also observed in the liver (Fig. S4D), kidney (Fig. S4E), spleen (Fig. S4F), and brain (Fig. S4G). Examination with SEM did not detect MWCNT-S in these organs.

Cytotoxicity in vitro. Smaller sized MWCNT were more potent than MWCNT-L in lowering cell viability of primary rat alveolar macrophages, human mesothelioma cells, human lung carcinoma cells, and human lung fibroblasts in vitro (Fig. S5).

Discussion

Multiwalled carbon nanotubes, when injected into the peritoneal cavity or the scrotum, results in the development of mesothelioma.[11–13] It is of great interest to know whether

pulmonary exposure leads to migration of MWCNT into the pleural cavity. Our previous study showed that short-term exposure of the lung to MWCNT resulted in fiber translocation into the pleural cavity and induction of pleural inflammation and fibrosis and mesothelial cell proliferation in the visceral pleura.[15] Similarly, Porter et al. and Mercer et al. showed that MWCNT could reach the visceral pleura[20] and enter the pleural cavity.[14] Furthermore, Mercer et al.[16] showed that MWCNT was transported to the muscle tissue of the chest wall and distant organs. Multiwalled carbon nanotubes were not found in the parietal pleura in these studies, probably due to short exposure periods and/or low doses.

Development of asbestos-induced pleural malignant mesothelioma in humans is a long-term process with a latency of up to tens of years,[2] indicating this is a cumulative effect of the fibers and associated pathogenic responses in the pleura. Thus, accurate modeling of human exposure to asbestos-like fibers and related pathogenesis in rodents is difficult. One solution to this problem is to increase exposure doses in animals. Therefore, in the present study, we sprayed a relatively high dose of MWCNT into the rat lung for a longer exposure period. The dosing was much higher than the recommended exposure limit of 1 μg/m^3 to carbon nanotubes and carbon nanofibers for an 8-h time–weight average proposed by the US National Institute of Occupational Safety and Health in 2013 (http://www.cdc.gov/niosh/docs/2013-145/).

— 67 —

Table 1. Cytokines/chemokines in the pleural cavity lavage and lung tissue of rats treated with multiwalled carbon nanotubes (MWCNT)

Cytokines/chemokines	Pleural cavity lavage (pg/mL)			Lung tissue (pg/mg protein)		
	PF68	MWCNT-L	MWCNT-S	PF68	MWCNT-L	MWCNT-S
G-CSF	n.d.	n.d.	n.d.	n.d.	n.d.	n.d.
GM-CSF	n.d.	n.d.	n.d.	n.d.	n.d.	n.d.
MIP1α	n.d.	n.d.	n.d.	63.8 ± 16.2	120.7 ± 21.0***	331.5 ± 90.4***,†††
MIP2	n.d.	n.d.	n.d.	12.4 ± 6.1	27.2 ± 4.9***	59.7 ± 16.7***,††
MCP1	n.d.	n.d.	n.d.	18.0 ± 13.9	39.1 ± 16.3*	213.1 ± 45.8***,†††
TNF-α	n.d.	n.d.	n.d.	n.d.	n.d.	n.d.
IFN-γ	n.d.	n.d.	n.d.	n.d.	n.d.	n.d.
GRO/KC	n.d.	n.d.	n.d.	425.2 ± 194.3	1105.4 ± 395.7**	1353.1 ± 362.6***
IP10	1.5 ± 1.5	8.9 ± 2.3***,†††	2.3 ± 2.3	35.6 ± 5.8	49.9 ± 4.4***	64.0 ± 11.0***,†
RANTES	3.8 ± 0.9	6.9 ± 1.9***,†††	4.1 ± 0.7	556.0 ± 128.6	531.7 ± 127.9††	335.4 ± 61.3**
IL-1α	n.d.	n.d.	n.d.	56.9 ± 14.4	85.3 ± 7.3**	84.5 ± 14.0**
IL-1β	n.d.	n.d.	n.d.	73.0 ± 19.3	103.7 ± 18.6*	154.5 ± 17.6***,†††
IL-4	n.d.	n.d.	n.d.	3.7 ± 3.0	4.2 ± 3.4	3.8 ± 1.9
IL-2	1.2 ± 1.9	14.1 ± 5.5***,††	5.2 ± 5.9	18.3 ± 4.1	18.9 ± 3.0	20.3 ± 7.7
IL-6	n.d.	n.d.	n.d.	29.1 ± 14.1	27.0 ± 13.5	32.6 ± 13.4
IL-12p70	n.d.	n.d.	n.d.	n.d.	n.d.	n.d.
IL-17α	n.d.	n.d.	n.d.	n.d.	n.d.	n.d.
IL-18	66.3 ± 17.0	108.4 ± 25.1**,†	70.4 ± 21.5	2294.8 ± 495.2	2471.8 ± 391.7	3085.6 ± 418.4*,†
VEGF	n.d.	n.d.	n.d.	111.0 ± 24.0	99.1 ± 14.4	201.4 ± 13.8***,†††
EGF	n.d.	n.d.	n.d.	n.d.	n.d.	n.d.

Data are expressed as mean ± standard deviation, n = 6 in each treatment group. *P < 0.05, **P < 0.01, ***P < 0.001, larger sized MWCNT (MWCNT-L; l = 8 μm, d = 150 nm) or smaller sized MWCNT (MWCNT-S; l = 3 μm, d = 15 nm) versus Pluronic F68 (PF68). †P < 0.05, ††P < 0.01, †††P < 0.001, MWCNT-L versus MWCNT-S. EGF, epidermal growth factor; G-CSF, granulocyte colony-stimulating factor; GM-CSF, granulocyte/macrophage colony-stimulating factor; GRO/KC, growth related oncogene/ keratinocyte-derived cytokine; IFNγ, γ-interferon; IL, interleukin; IP-10, interferon gamma-induced protein 10; n.d., not detectable; TNF-α, tumor necrosis factor-α; MCP1, monocyte chemotactic protein 1; MIP, macrophage inflammatory protein; RANTES, regulated on activation, normal T cell expressed and secreted; VEGF, vascular endothelial growth factor.

The results of this study show that MWCNT-L applied to the lung was found in the pleural cavity and deposited in the parietal pleura, and induced higher inflammatory reactions in the pleural cavity, fibrotic thickening of both the parietal and visceral pleura, and mesothelial proliferation, whereas MWCNT-S caused higher inflammatory reactions and 8-OHdG formation in the lung. Reports have shown that pro-inflammatory cytokines promote mesothelial cell transformation in vitro,[21] indicating chronic inflammation is a likely contributing factor in the development of mesothelioma. Due to its length and needle-like shape, MWCNT-L deposited in the pleura, especially in the parietal side, is difficult to clear and results in chronic inflammation in the deposited site. Thus, MWCNT-L has more potential to cause pleural mesothelioma.

It should be noted that properties of MWCNT-L and MWCNT-S, other than size and shape, such as chemical composition (MWCNT-L contains zinc [Fig. S1]) and rigidity,[22] may contribute to the observed different effects in the pleura and lung. Smaller sized MWCNT were not found in the pleural cavity, possibly because MWCNT-S formed cotton candy-like aggregates and very few free fibers translocated from the lung to the pleural cavity, or/and these fibers were rapidly cleared from the pleural cavity. The size- and shape-dependent pleural toxicity shown in our study is consistent with previous reports that direct injection of MWCNT into the pleural cavity leads to length-dependent retention of MWCNT in the pleural cavity and sustained inflammation and fibrosis in the parietal pleura,[17] and with reports that inhaled amosite fibers are found in the parietal pleura with inflammation and fibrosis.[23,24] When we were preparing this manuscript, Murphy et al. reported that long MWCNT aspired into the lung of

mice was found in the parietal pleura and caused stronger inflammation and fibrosis both in the pleura and lung than short or tangled MWCNT. The lung responses to short or tangled MWCNT are different from our results, possibly due to different animals, administration methods, MWCNT used, and sampling time.[25]

Current administration regulations to set permissible air concentrations of particles and fibers are usually based on lung burdens. Although lung diseases may well be related to the lung burden of specific particles or fibers, lung burden is not always suitable for prediction of pleural toxicity of asbestos-like materials.[2,7] In the present study, MWCNT-S showed higher toxicity in the lung, whereas MWCNT-L was more toxic in the pleural tissue, indicating that the site of deposition and the associated toxicity needs be taken into account in regulating carbon nanotube exposure.

In conclusion, deposition of MWCNT-L and induction of fibrosis and mesothelial cell proliferation in the parietal pleura indicate that larger sized MWCNT has greater potential to induce asbestos-like pleural lesions.

Acknowledgments

Disclosure Statement
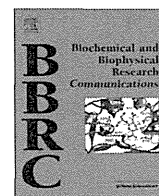
The authors have no conflict of interests.

References

1 Boutin C, Rey F, Gouvernet J, Viallat JR, Astoul P, Ledoray V. Thoracoscopy in pleural malignant mesothelioma: a prospective study of 188 consecutive patients. Part 2: prognosis and staging. *Cancer* 1993; **72**: 394–404.

2 Cugell DW, Kamp DW. Asbestos and the pleura: a review. *Chest* 2004; **125**: 1103–17.

3 Kane AB. Mechanisms of mineral fibre carcinogenesis. *IARC Sci Publ* 1996; **140**: 11–34.

4 Robinson BW, Musk AW, Lake RA. Malignant mesothelioma. *Lancet* 2005; **366**: 397–408.

5 Boutin C, Dumortier P, Rey F, Viallat JR, De Vuyst P. Black spots concentrate oncogenic asbestos fibers in the parietal pleura. Thoracoscopic and mineralogic study. *Am J Respir Crit Care Med* 1996; **153**: 444–9.

6 Kohyama N, Suzuki Y. Analysis of asbestos fibers in lung parenchyma, pleural plaques, and mesothelioma tissues of North American insulation workers. *Ann N Y Acad Sci* 1991; **643**: 27–52.

7 Donaldson K, Murphy FA, Duffin R, Poland CA. Asbestos, carbon nanotubes and the pleural mesothelium: a review of the hypothesis regarding the role of long fibre retention in the parietal pleura, inflammation and mesothelioma. *Part Fibre Toxicol* 2010; **7**: 5.

8 Bonner JC. Nanoparticles as a potential cause of pleural and interstitial lung disease. *Proc Am Thorac Soc* 2010; **7**: 138–41.

9 Nagai H, Toyokuni S. Biopersistent fiber-induced inflammation and carcinogenesis: lessons learned from asbestos toward safety of fibrous nanomaterials. *Arch Biochem Biophys* 2010; **502**(1): 1–7.

10 Poland CA, Duffin R, Kinloch I *et al.* Carbon nanotubes introduced into the abdominal cavity of mice show asbestos-like pathogenicity in a pilot study. *Nat Nanotechnol* 2008; **3**: 423–8.

11 Sakamoto Y, Nakae D, Fukumori N *et al.* Induction of mesothelioma by a single intrascrotal administration of multi-wall carbon nanotube in intact male Fischer 344 rats. *J Toxicol Sci* 2009; **34**(1): 65–76.

12 Takagi A, Hirose A, Futakuchi M, Tsuda H, Kanno J. Dose-dependent mesothelioma induction by intraperitoneal administration of multi-wall carbon nanotubes in p53 heterozygous mice. *Cancer Sci* 2012; **103**: 1440–4.

13 Takagi A, Hirose A, Nishimura T *et al.* Induction of mesothelioma in p53+/− mouse by intraperitoneal application of multi-wall carbon nanotube. *J Toxicol Sci* 2008; **33**: 105–16.

14 Mercer RR, Hubbs AF, Scabilloni JF *et al.* Distribution and persistence of pleural penetrations by multi-walled carbon nanotubes. *Part Fibre Toxicol* 2010; **7**: 28.

15 Xu J, Futakuchi M, Shimizu H *et al.* Multi-walled carbon nanotubes translocate into the pleural cavity and induce visceral mesothelial proliferation in rats. *Cancer Sci* 2012; **103**: 2045–50.

16 Mercer RR, Scabilloni JF, Hubbs AF *et al.* Extrapulmonary transport of MWCNT following inhalation exposure. *Part Fibre Toxicol* 2013; **10**(1): 38.

17 Murphy FA, Poland CA, Duffin R *et al.* Length-dependent retention of carbon nanotubes in the pleural space of mice initiates sustained inflammation and progressive fibrosis on the parietal pleura. *Am J Pathol* 2011; **178**: 2587–600.

18 Schinwald A, Murphy FA, Prina-Mello A *et al.* The threshold length for fiber-induced acute pleural inflammation: shedding light on the early events in asbestos-induced mesothelioma. *Toxicol Sci* 2012; **128**: 461–70.

19 Xu J, Futakuchi M, Iigo M *et al.* Involvement of macrophage inflammatory protein 1alpha (MIP1alpha) in promotion of rat lung and mammary carcinogenic activity of nanoscale titanium dioxide particles administered by intrapulmonary spraying. *Carcinogenesis* 2010; **31**: 927–35.

20 Porter DW, Hubbs AF, Mercer RR *et al.* Mouse pulmonary dose- and time course-responses induced by exposure to multi-walled carbon nanotubes. *Toxicology* 2010; **269**: 136–47.

21 Wang ZL. Functional oxide nanobelts: materials, properties and potential applications in nanosystems and biotechnology. *Annu Rev Phys Chem* 2004; **55**: 159–96.

22 Nagai H, Okazaki Y, Chew SH *et al.* Diameter and rigidity of multiwalled carbon nanotubes are critical factors in mesothelial injury and carcinogenesis. *Proc Natl Acad Sci U S A* 2011; **108**: E1330–8.

23 Bernstein DM, Rogers RA, Sepulveda R *et al.* The pathological response and fate in the lung and pleura of chrysotile in combination with fine particles compared to amosite asbestos following short-term inhalation exposure: interim results. *Inhal Toxicol* 2010; **22**: 937–62.

24 Bernstein DM, Rogers RA, Sepulveda R *et al.* Quantification of the pathological response and fate in the lung and pleura of chrysotile in combination with fine particles compared to amosite-asbestos following short-term inhalation exposure. *Inhal Toxicol* 2011; **23**: 372–91.

25 Murphy FA, Poland CA, Duffin R, Donaldson K. Length-dependent pleural inflammation and parietal pleural responses after deposition of carbon nanotubes in the pulmonary airspaces of mice. *Nanotoxicology* 2013; **7**: 1157–67.

Supporting Information

Additional supporting information may be found in the online version of this article:

Fig. S1. Characterization of multiwalled carbon nanotubes.

Fig. S2. Determination of the thickness of the pleura in rats treated with multiwalled carbon nanotubes.

Fig. S3. Granuloma formation, alveolar macrophage infiltration, and 8-hydroxydeoxyguanosine (8-OHdG) induction in the lung.

Fig. S4. Transportation of larger sized multiwalled carbon nanotubes to extrapulmonary organs.

Fig. S5. Cytotoxicity of multiwalled carbon nanotubes *in vitro.*

Contents lists available at ScienceDirect

Biochemical and Biophysical Research Communications

High-temperature calcined fullerene nanowhiskers as well as long needle-like multi-wall carbon nanotubes have abilities to induce NLRP3-mediated IL-1β secretion

CrossMark

Hongyan Cui [a], Weijia Wu [a], Keiichiro Okuhira [a], Kun'ichi Miyazawa [b], Takayuki Hattori [a], Kimie Sai [a], Mikihiko Naito [a], Kazuhiro Suzuki [a], Tetsuji Nishimura [a], Yoshimitsu Sakamoto [c], Akio Ogata [c], Tomokazu Maeno [c], Akiko Inomata [c], Dai Nakae [c], Akihiko Hirose [a], Tomoko Nishimaki-Mogami [a],*

[a] Division of Biochemistry and Metabolism, Division of Biochemistry and Molecular Biology, Division of Environmental Chemistry, Division of Risk Assessment, and Biological Safety Research Center, National Institute of Health Sciences, Tokyo 158-8501, Japan
[b] Fullerene Engineering Group, Materials Processing Unit, National Institute for Materials Science, Tsukuba, Ibaraki 305-0044, Japan
[c] Department of Environmental Health and Toxicology, Tokyo Metropolitan Institute of Public Health, Tokyo 169-0073, Japan

ARTICLE INFO

ABSTRACT

Because multi-wall carbon nanotubes (MWCNTs) have asbestos-like shape and size, concerns about their pathogenicity have been raised. Contaminated metals of MWCNTs may also be responsible for their toxicity. In this study, we employed high-temperature calcined fullerene nanowhiskers (HTCFNWs), which are needle-like nanofibers composed of amorphous carbon having similar sizes to MWCNTs but neither metal impurities nor tubular structures, and investigated their ability to induce production a major proinflammatory cytokine IL-1β via the Nod-like receptor pyrin domain containing 3 (NLRP3)-containing flammasome-mediated mechanism. When exposed to THP-1 macrophages, long-HTCFNW exhibited robust IL-1β production as long and needle-like MWCNTs did, but short-HTCFNW caused very small effect. IL-1β release induced by long-HTCFNW as well as by long, needle-like MWCNTs was abolished by a caspase-1 inhibitor or siRNA-knockdown of NLRP3, indicating that NLRP3-inflammasome-mediated IL-1β production by these carbon nanofibers. Our findings indicate that the needle-like shape and length, but neither metal impurities nor tubular structures of MWCNTs were critical to robust NLRP3 activation.

© 2014 Elsevier Inc. All rights reserved.

1. Introduction

Carbon nanotubes (CNTs) are increasingly being used in various industrial fields because of their unique electronic and mechanical properties. However, these unique physicochemical properties, especially the asbestos-like shape and size with a high-aspect ratio, are currently of great concern with respect to the environment and human health [1]. A variety of multiwall carbon nanotubes (MWCNTs) and single-wall carbon nanotubes have been produced, and some of these materials have been shown to cause mesothelioma after injection into the abdominal cavities of p53+/− mice [2]

or the scrotum of wild-type rats [3]. Inflammatory cell recruitment and granulomas [4] and elevated mRNA expression of pro-inflammatory cytokines and chemokines in peritoneal cells [5] were induced by MWCNTs injected into the abdominal cavities of mice. Pulmonary exposed MWCNTs were shown to reach subpleural tissue and macrophages in mice and rats and to induce fibrosis, inflammation, allergic immune responses [6–8] and mesothelial proliferation [9]. Abundant inflammatory cell infiltration and increased pro-inflammatory cytokine levels in the pleural cavity were also observed [9,10].

IL-1β is an important proinflammatory cytokine that is generated at sites of injury, infection, or immunological challenge to recruit immune cells [11]. It is very likely that IL-1β plays a major role in MWCNT-induced inflammation or immune responses. Recent studies have revealed that IL-1β maturation and release are controlled by a large multiprotein complex, called the inflammasome [11]. In particular, the inflammasome containing the Nod-like receptor (NLR)-family protein 3, NLRP3, can be activated

by a variety of danger signals or phagocytosed crystals and aggregated proteins and has been implicated in several chronic inflammatory diseases [11,12]. Certain MWCNTs have been shown to induce NLRP3-mediated IL-1β secretion [13,14]. Various MWCNTs with different physicochemical properties, including length, diameter, and contaminant metals, are produced. However, factors that are critical to inducing NLRP3 activation and/or IL-1β production remain unclear.

Shape and size of MWCNTs similar to asbestos have been implicated in their toxicity. In addition, several studies have suggested that metal contamination, which is derived from catalysts used in the synthesis of CNTs, is responsible for cytotoxicity and genotoxicity of MWCNTs [15–18] and for the redox-dependent response of macrophages [19], although this suggestion remains controversial [4,20].

In this study, we employed high-temperature calcined fullerene nanowhiskers (HTCFNWs), which are amorphous carbon nanofibers and have a needle-like morphology with similar length to MWCNTs [21]. Notably, HTCFNWs do not contain metal impurities, because they are produced from fullerene nanowhiskers by heating in vacuum [21]. Fullerene nanowhiskers are thin, single crystal nanofibers composed of C_{60} fullerene molecules that are bound via van der Waals forces [22]. We investigated the ability of long or short HTCFNW, which did not contain tubular structures and metal impurities, and various MWCNTs with different physical properties to induce IL-1β secretion, and sought to identify factors required for inducing NLRP3-mediated IL-1β release.

2. Materials and methods

2.1. Materials

We used three types of MWCNT grown in the vapor phase (Fig. 1A): MWCNT-M was provided by Nanocarbon Technologies Co., Ltd. (Tokyo, Japan). MWCNT-SD1 and MWCNT-SD2 were by Showa-Denko Co., Ltd. (Tokyo, Japan). HTCFNW-L and -S were prepared by heating fullerene nanowhiskers at 900 °C in vacuum [21]. Fullerene nanowhiskers were synthesized from C_{60} fullerene by a liquid–liquid interfacial precipitation method [23]. The size distribution of MWCNTs and HTCFNWs was determined by scanning electron microscopy. Fe contents were determined by a collision type inductively coupled plasma mass spectrometer as described [2].

2.2. Preparation of MWCNT and HTCFNW dispersions

MWCNTs were suspended in phosphate-buffered saline (PBS) containing 0.5% Tween-20 (or Tween-80) at a concentration of 0.5 mg/mL, sonicated with a bath-type sonicator (BRNSON 1200) for 1 min × 3, and then diluted with PBS to a concentration of 0.2 mg/mL. The suspension of carbon nanotubes was homogenized by passing through a 30G needle. HTCFNWs (0.5 mg/mL) were dispersed in 0.1% Tween 80.

2.3. Cell culture and treatment of cells with HTCFNWs and MWCNTs

THP-1 cells (obtained from American Type Culture Collection (ATCC), Manassas, VA) were maintained in RPM-1 medium containing 10% fetal bovine serum (FBS). Cells were plated at a density of 3.5×10^5 cells in 24 well plates, differentiated for 72 h with 0.3 μM PMA, and further incubated for 24 h without PMA. The cells were treated for 6 h with carbon nanomaterials or the indicated stimuli. As indicated, 10 μM of caspase-1 inhibitor z-YVAD-fmk (Calbiochem), 0.2 μM cytochalasin D (Sigma), 130 mM KCl, 3 mM ATP, or 3.4 μM nigericin (Sigma) was added to the incubation

medium. Cell extract and the medium supernatant were collected for analysis of their cytokine content. Cell viability was assessed by release of LDH to the medium (with a Cytotoxicity Detection Kit Plus (Roche)) or by the Tetracolor one cell proliferation assay, which detects vital mitochondrial function (Seikagaku Kogyo Ltd., Tokyo).

2.4. Analysis of IL-1β secretion

IL-1β in the medium supernatant was analyzed by the Milliplex immunoassay (Merck Co., Ltd.) according to the manufacturer's protocol or by Western blotting.

2.5. Flow cytometry analysis to detect cellular uptake of MWCNTs and HTCFNWs

PMA-differentiated THP-1 cells were exposed to MWCNTs or HTCFNWs for 20 h. The cells were washed, trypsinized, suspended in PBS containing 10% FBS, and filtered through 100 μm nylon mesh. The uptake of carbon nanofibers was determined by flow cytometry (FACSCalibur™; BD Biosciences) measuring side scatter (SSC) and forward scatter (FSC) of 10,000 counts.

2.6. Western blotting

Cells were extracted with RIPA containing the protease inhibitor cocktail set III (1:100) (Calbiochem). The culture medium supernatant was concentrated with a Microkon Ultracel YM-10 (10 kDa cut-off; Millipore, Bedford, MA) or Amicon Ultra-3K (3 kDa cut-off; Millipore, Bedford, MA). Cell extract and medium samples were analyzed by polyacrylamide gel electrophoresis followed by transfer to an Immobilon-P Transfer Membrane (Millipore). Anti IL-1β antibody (sc-7884), anti-caspase-1 P-10 antibody (sc-515) (Santa Cruz Biotechnology, Inc), and anti β-actin antibody (Sigma) were used. The immunoreactive proteins were visualized using ECL (GE Healthcare, Piscataway, NJ) or a SuperSignal West Femto Substrate kit (Thermo Scientific, Rockford, IL), and light emission was quantified with a LAS-3000 lumino-image analyzer (Fuji, Tokyo, Japan).

2.7. NLRP3 knockdown by RNA interference

THP-1 cells were plated at a density of 1.75×10^6 cells in 12 well plates and were differentiated for 72 h with 0.3 μM PMA. Cells were transiently transfected with gene-specific StealthTM Select RNAi or Stealth RNAi negative control (Invitrogen, Carlsbad, CA) using lipofectamine RNAi MAX reagent (Invitrogen) for 24 h. The Stealth RNAi sequences used were human NLRP3 sense1 (5′-AACCCAGGCACACUCCUCCUGUAGC-3′), antisense1 (5′-GCUACAG GAGGAGUGUGCCUGGGUU-3′); sense2 (5′-UUCUGUUGCUGGCUU CCUCAGCACA-3′), antisense2 (5′-UGUGCUGAGGAAGCCAGCAACA GAA-3′); sense3 (5′-UCCUGUGCUACUCCAGUAACCCAGG-3′), and antisense3 (5′-CCUGGGUUACUGGAGUAGCACAGGA-3′).

2.8. RNA extraction and quantitative real-time RT-PCR

Total RNA was extracted with an RNeasy Mini Kit using on-column deoxyribonuclease digestion to eliminate genomic DNA contamination according to the manufacturer's instructions (Qiagen, Valencia, CA). Quantitative real-time RT-PCR was performed with an ABI Prism 7300 sequence detection system using the TaqMan one-step RT-PCR Master Mix Reagent Kit (Applied Biosystems, Foster City, CA) with TaqMan probes/primers as follows: human NLRP3, forward: 5′-TGAGCCTCAACAAACGCTACA-3′; reverse: 5′-CTTGCCGATGGCCAGAAG -3′; probe: 5′-FAM-CTGCGTCTCATCAAG GAGCACCGG-BHQ-3′. 18S rRNA (Applied Biosystems). Expression

data were normalized to 18S rRNA levels, and are presented as the fold difference between treated and untreated cells.

2.9. Statistical analysis

Data were analyzed by ANOVA followed by the Student–New-man–Keuls method. Statistical significance was established at the $P < 0.05$ level.

3. Results

3.1. HTCFNWs and various MWCNTs display different abilities to induce IL-1β production

HTCFNWs are the fullerene nanowhiskers heat-treated in vacuum at 900 °C and are composed of amorphous carbon [21]. Two types of HTCFNWs with different lengths and diameters (Fig. 1A) were examined for their ability to induce IL-1β production compared with MWCNT-SD1 in the human macrophage-like cell line THP-1 cells. As shown in Fig. 1B left, long HTCFNWs (HTCFNW-L) caused robust IL-1β production in a dose-dependent manner, which corresponded to ca. 30% of the MWCNT-SD1-induced stimulation at the same concentration. Short HTCFNWs (HTCFNW-S) had a very small but significant and phagocytosis-dependent effect (Fig. 1B right). We also investigated the ability of various MWCNTs with different physical properties (Fig. 1A) to stimulate IL-1β production. MWCNT-M, -SD1, or -SD2 dose-dependently induced IL-1β secretion into the medium (Fig. 1C). IL-1β production induced by MWCNT-M or -SD1 was almost completely inhibited by pretreating cells with the phagocytosis inhibitor cytochalasin D that impairs the actin filament assembly (Fig. 1D), indicating that the uptake of MWCNTs into cells is required for stimulation of IL-1β production.

These findings clearly show that MWCNTs with various physical properties exhibit different abilities to induce IL-1β production, and HTCFNWs without impurities exhibited a comparable effect to MWCNTs.
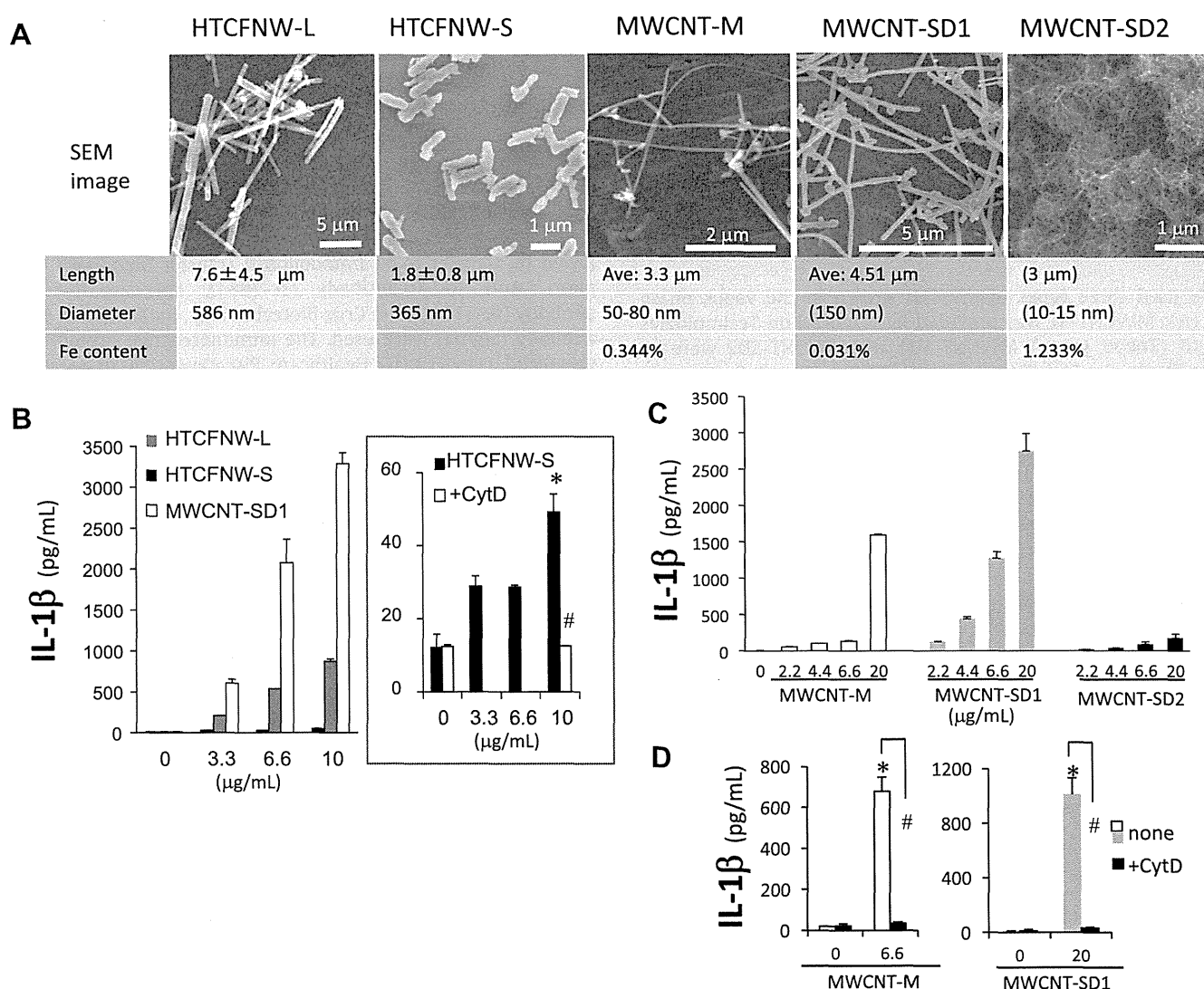

Fig. 1. HTCFNWs as well as long-, needle-like MWCNTs have abilities to induce IL-1β production. (A) Specification of the HTCFNWs and MWCNTs used in this study. Characteristics in parenthesis were provided by manufacturers. (B–D) THP-1 cells were stimulated for 6 h with the indicated amount (μg/mL of media) of HTCFNW-L, -S, and MWCNT-SD1 dispersed in Tween 80 (final concentration, 0.002%), or MWCNT-M, -SD1, and -SD2 dispersed in Tween 20 (final concentration, 0.002%) (C, D). Phagocytosis was inhibited by treating cells with cytochalasin D (0.2 μM) for 30 min before stimulation. IL-1β in the medium was analyzed by the Milliplex immunoassay. Data represent means ± S.D (n = 2). Significant difference from vehicle control (*) or between cytochalasin D-untreated and -treated cells (#). A vertical axis for a HTCFNW-S graph was expanded in the right panel (B).

Internalization of nanofibers by cells was evaluated with the SSC value from flow cytometry. The SSC is directly related to cell granularity and is used as a measurement of the uptake of particles or nanofibers [24,25]. Exposure of cells to MWCNT-SD1 or MWCNT-M resulted in increases in the SSC values (Fig. 2A and B), which were inhibited by the phagocytosis inhibitor cytochalasin D (Fig. 2C). MWCNT-SD2, with an agglomerate morphology, had no effect. HTCFNW-L and -S caused similar levels of SSC increase (Fig. 2D).

3.2. HTCFNW as well as MWCNTs promote caspase-1 cleavage via NLRP3 activation

The mature form of IL-1β is cleaved from the pro-IL-1β precursor by caspase-1. As shown in Fig. 3A, MWCNT-SD1 induced a potent, dose-responsive release of mature IL-1β (p17) to the medium, which was accompanied by an increase in the active caspase-1 fragment (p10). As a positive control, we confirmed that the bacterial ionophore nigericin promoted caspase-1 cleavage and IL-1β maturation. Furthermore, IL-1β secretion induced by MWCNT-M was completely inhibited by the caspase-1-inhibitor zYVAD-fmk (Fig. 3B). IL-1β release induced by MWCNT-SD1 (Fig. 3C) and HTCFNW-L (Fig. 3D) was similarly repressed by zYVAD-fmk. These findings indicate that HTCFNW-L, as well as needle-like MWCNTs, induces activation of caspase-1.

Caspase-1 is auto-activated by a signal within the multiprotein complex known as the "inflammasome" [11]. We examined whether the NLRP3-containing inflammasome is involved in MWCNT-induced IL-1β production. NLRP3 inflammasome activation is known to require potassium (K+) efflux [11]. As reported that asbestos-induced secretion of mature IL-1β was repressed by a high concentration of KCl added to the medium to inhibit K+ efflux [26], MWCNT-M-induced IL-1β secretion was blocked by KCl in the medium (Fig. 3B).

To test the role of NLRP3, siRNA knockdown of NLRP3 was performed. In THP-1 cells, three different siRNAs against NLRP3 effectively reduced NLRP3 mRNA expression (Fig. 4A). MWCNT-M-induced IL-1β secretion, determined by immunoassay, was effectively reduced by three different NLRP3 siRNAs (Fig. 4C). This reduction was accompanied by reductions of the active form of capsase-1 (p10) and cleaved IL-1β into the medium (Fig. 4B). IL-1β secretion elicited by MWCNT-SD1 or HTCFNW-L was also diminished by the NLRP3 siRNA (Fig. 4D and E). These findings clearly demonstrate that NLRP3 is involved in IL-1β maturation induced by HTCFNW-L as well as needle-like MWCNTs.

4. Discussion

In this study, we showed that fullerene-derived HTCFNWs and certain MWCNTs, with a long, needle like morphology potently
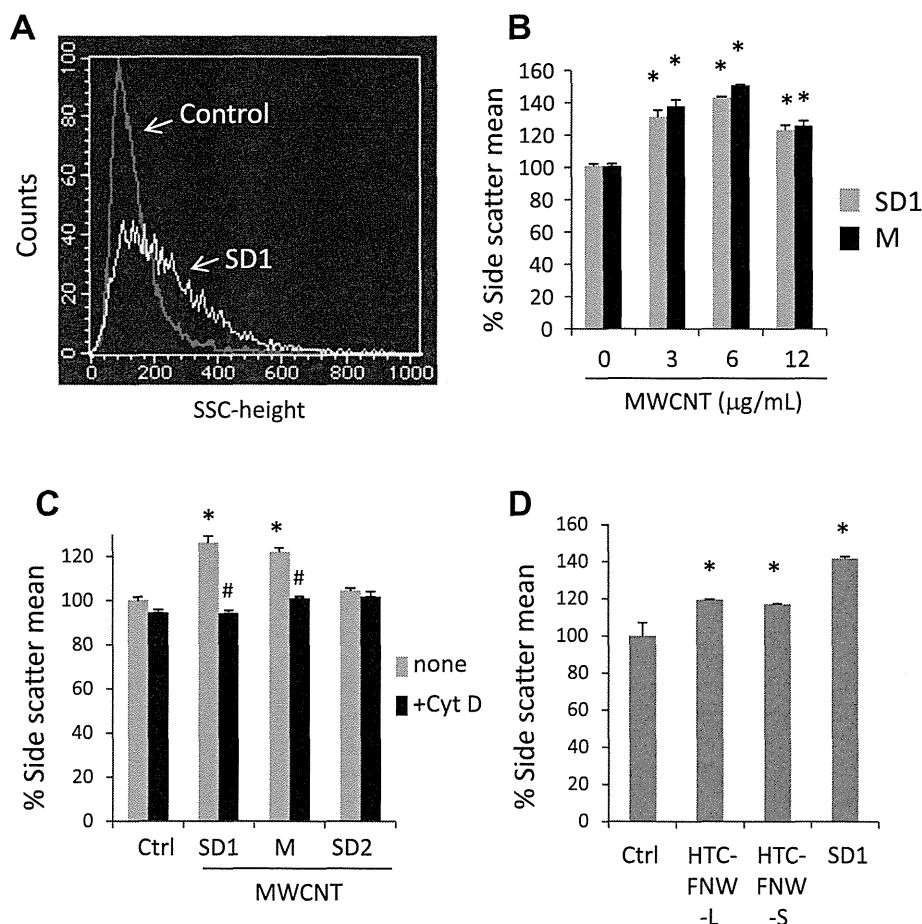

Fig. 2. Flow cytometry analysis shows cell internalization of MWCNTs and HTCFNWs. THP-1 cells were treated with or without cytochalasin D (0.2 µM) for 30 min and were then exposed to the indicated concentration of MWCNT-SD1, -SD2, -M, HTCFNW-L or -S dispersed in Tween 80 (final concentration, 0.002%) for 20 h. The cells were trypsinized and analyzed by flow cytometry. (A) Representative histogram shows the cell count vs side scatter (SSC) for cells treated without (gray line) or with MWCNT-SD1 (6 µg/mL) (white line). (B–D) Mean of the SSC value of cells treated without or with increasing concentrations of MWCNT-SD1 or -M (B), or 6 µg/mL of MWCNTs or HTCFNWs (C, D). Uptake was detectable as an increase in cell number with higher SSC. Data represent means ± S.D (n = 2 or 3). Significant difference from vehicle control (*) or between cytochalasin D-untreated and -treated cells (#).
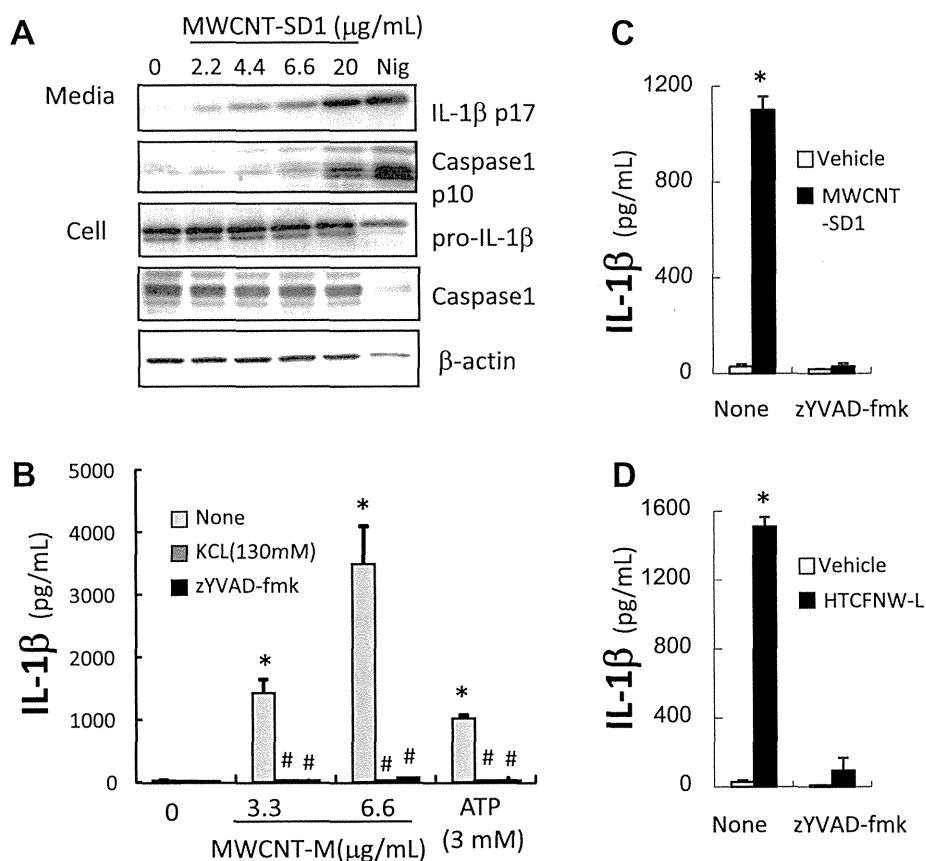
Fig. 3. MWCNT- and HTCFNW-induced IL-1β secretion accompanies caspase-1 cleavage and is repressed by extracellular KCl (130 mM) or a caspase-1 inhibitor. (A) THP-1 cells were stimulated for 6 h with the indicated amount (μg/mL of media) of MWCNT-SD1 dispersed in 0.002% Tween 20 or nigericin (Nig) (3.4 μM). The cell lysate and medium were analyzed by immunoblotting. (B–D) THP-1 cells were treated for 6 h with MWCNT-M or ATP (3 mM) (B), or MWCNT-SD1 (10 μg/mL) (C) and HTCFNW-L (10 μg/mL) (D) dispersed in 0.002% Tween 80 in the presence or absence of 130 mM KCl or the caspase-1 inhibitor zYVAD-fmk (10 μM). IL-1β in the medium was analyzed by the Milliplex immunoassay. Data represent means ± S.D (n = 2). Significant difference from vehicle control (*) or between inhibitor-untreated and -treated cells (#).

induce proinflammatory cytokine IL-1β production in human macrophage-like THP-1 cells (Fig. 1). Prominent IL-1β release by these nanomaterials was sensitive to the phagocytosis inhibitor cytochalasin D (Fig. 1B) and was accompanied by increases in cellular SSC values related to particle internalization (Fig. 2). Notably, HTCFNW-L and -S produced a potent and faint IL-1β release, respectively (Fig. 1C), whereas both fibers caused similar changes in the cellular SSC level (Fig. 2D). These findings clearly indicate that the needle-like shape and length of carbon nanofibers are critical to inducing IL-1β release after being taken up by cells.

The prominent IL-1β production by MWCNT-M, MWCNT-SD1, and HTCFNW-L was repressed by a high concentration of potassium or caspase-1 inhibitor and was accompanied by an increase in the active-form of caspase-1 release. Knockdown of NLRP3 by specific siRNAs diminished IL-1β production induced by these nanofibers, indicating that the NLRP3-containing inflammasome is involved in IL-1β release induced by fullerene-derived HTCFNW-L as well as long, needle-like MWCNTs.

NLRP3 is known to be activated by a variety of danger signals, including endogenous crystals of monosodium urate and cholesterol, exogenous silica crystals, aluminum salts, carbon nanotubes, and bacterial toxins, and the complex plays a critical role in IL-1β-mediated pathology [11,12]. Although the mechanism of NLRP3 activation is still unclear, potassium efflux, ROS generation, and lysosome destabilization have been implicated in NLRP3-inflammasome activation [11,12]. Changes in the redox environment have been suggested to modulate the NLRP3 inflammasome

activation potential [27]. Our findings indicate that the ability of HTCFNW-L to induce NLRP3-mediated IL-1β release is comparable to that of MWCNT-M and -SD1. HTCFNWs have a needle-like morphology and similar size to MWCNT-M and -SD1. However, unlike MWCNTs, HTCFNWs contain no tubular structures or metal impurities such as Fe or Ni. Previous studies have suggested that metal contamination of CNTs is responsible for their toxicity [16–18] and cellular redox-response [19]. Importantly, HTCFNW-L and -S, which were synthesized from pure fullerene by liquid–liquid interfacial precipitation methods [23] followed by sintering with heat-treatment, contain no metal impurities. Thus, our findings clearly demonstrate that long, needle-like structures of MWCNTs and HTCFNW-L, but not metal contaminants, are required for NLRP3 inflammasome activation leading to the resulting IL-1β release.

The NLPR3-inflamasome has been implicated in several chronic inflammatory diseases such as metabolic syndrome, inflammatory bowel disease, atherosclerosis, and Alzheimer disease, as well as in regulating antimicrobial and mucosal immune responses [12,28]. Our findings raise concerns that MWCNTs may affect these diseases and responses through stimulating NLRP3-mediated IL-1β production.

In conclusion, we have shown for the first time that fullerene-derived HTCFNW-L as well as MWCNTs induces IL-1β release in an NLRP3-mediated process. Our findings indicate that the needle-like shape and length of MWCNTs, but not metal impurities or tubular structures, play a critical role in robust NLRP3 activation, which is closely implicated in chronic inflammatory diseases.
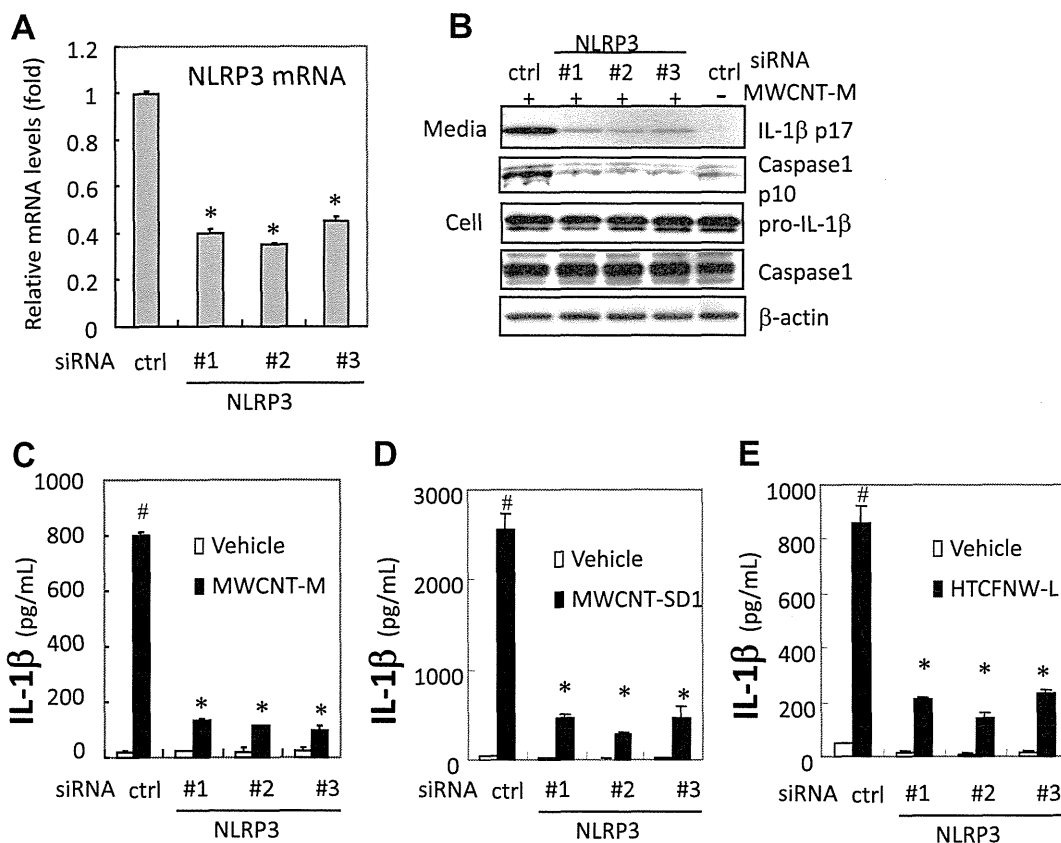
Fig. 4. Knockdown of NLRP3 diminishes MWCNT- and HTCFNW-elicited IL-1β secretion. THP-1 cells were transfected with either siRNA against three different sequences of NLRP3 (#1–3) or a negative control siRNA. After 24 h, cells were treated with MWCNT-M (6.6 µg/mL) (B, C), MWCNT-SD1 (10 µg/mL) (D) dispersed in 0.002% Tween 20, or HTCFNW-L (10 µg/mL) in Tween 80 (E) for 6 h. (A) NLRP3 mRNA levels were measured by quantitative real-time RT-PCR analysis normalized with the 18S rRNA. (B) IL-1β (p17) and caspase-1 (p10) in the medium and pro-IL-1β and caspase-1 in the cell lysate were analyzed by immunoblotting. (C–E) IL-1β in the medium was analyzed by the Milliplex immunoassay. Data represent means ± S.D. (n = 3 or 2). Significant difference from vehicle-treated control (#) or control siRNA-transfected cells (*).
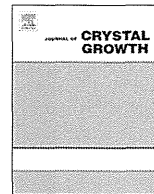
Acknowledgments

References

[1] K. Donaldson, R. Aitken, L. Tran, V. Stone, R. Duffin, G. Forrest, A. Alexander, Carbon nanotubes: a review of their properties in relation to pulmonary toxicology and workplace safety, Toxicol. Sci. 92 (2006) 5–22.

[2] A. Takagi, A. Hirose, T. Nishimura, N. Fukumori, A. Ogata, N. Ohashi, S. Kitajima, J. Kanno, Induction of mesothelioma in p53+/- mouse by intraperitoneal application of multi-wall carbon nanotube, J. Toxicol. Sci. 33 (2008) 105–116.

[3] Y. Sakamoto, D. Nakae, N. Fukumori, K. Tayama, A. Maekawa, K. Imai, A. Hirose, T. Nishimura, N. Ohashi, A. Ogata, Induction of mesothelioma by a single intrascrotal administration of multi-wall carbon nanotube in intact male Fischer 344 rats, J. Toxicol. Sci. 34 (2009) 65–76.

[4] C.A. Poland, R. Duffin, I. Kinloch, A. Maynard, W.A. Wallace, A. Seaton, V. Stone, S. Brown, W. Macnee, K. Donaldson, Carbon nanotubes introduced into the abdominal cavity of mice show asbestos-like pathogenicity in a pilot study, Nat. Nanotechnol. 3 (2008) 423–428.

[5] A. Yamaguchi, T. Fujitani, K. Ohyama, D. Nakae, A. Hirose, T. Nishimura, A. Ogata, Effects of sustained stimulation with multi-wall carbon nanotubes on immune and inflammatory responses in mice, J. Toxicol. Sci. 37 (2012) 177–189.

[6] D.W. Porter, A.F. Hubbs, R.R. Mercer, N. Wu, M.G. Wolfarth, K. Sriram, S. Leonard, L. Battelli, D. Schwegler-Berry, S. Friend, M. Andrew, B.T. Chen, S. Tsuruoka, M. Endo, V. Castranova, Mouse pulmonary dose- and time course-responses induced by exposure to multi-walled carbon nanotubes, Toxicology 269 (2010) 136–147.

[7] P. Ravichandran, S. Baluchamy, R. Gopikrishnan, S. Biradar, V. Ramesh, V. Goornavar, R. Thomas, B.L. Wilson, R. Jeffers, J.C. Hall, G.T. Ramesh, Pulmonary

biocompatibility assessment of inhaled single-wall and multiwall carbon nanotubes in BALB/c mice, J. Biol. Chem. 286 (2011) 29725–29733.

[8] J.P. Ryman-Rasmussen, M.F. Cesta, A.R. Brody, J.K. Shipley-Phillips, J.I. Everitt, E.W. Tewksbury, O.R. Moss, B.A. Wong, D.E. Dodd, M.E. Andersen, J.C. Bonner, Inhaled carbon nanotubes reach the subpleural tissue in mice, Nat. Nanotechnol. 4 (2009) 747–751.

[9] J. Xu, M. Futakuchi, H. Shimizu, D.B. Alexander, K. Yanagihara, K. Fukamachi, M. Suzui, J. Kanno, A. Hirose, A. Ogata, Y. Sakamoto, D. Nakae, T. Omori, H. Tsuda, Multi-walled carbon nanotubes translocate into the pleural cavity and induce visceral mesothelial proliferation in rats, Cancer Sci. 103 (2012) 2045–2050.

[10] E.J. Park, W.S. Cho, J. Jeong, J. Yi, K. Choi, K. Park, Pro-inflammatory and potential allergic responses resulting from B cell activation in mice treated with multi-walled carbon nanotubes by intratracheal instillation, Toxicology 259 (2009) 113–121.

[11] K. Schroder, J. Tschopp, The inflammasomes, Cell 140 (2010) 821–832.

[12] T. Strowig, J. Henao-Mejia, E. Elinav, R. Flavell, Inflammasomes in health and disease, Nature 481 (2012) 278–286.

[13] E. Meunier, A. Coste, D. Olagnier, H. Authier, L. Lefevre, C. Dardenne, J. Bernad, M. Beraud, E. Flahaut, B. Pipy, Double-walled carbon nanotubes trigger IL-1beta release in human monocytes through Nlrp3 inflammasome activation, Nanomedicine 8 (2012) 987–995.

[14] J. Palomaki, E. Valimaki, J. Sund, M. Vippola, P.A. Clausen, K.A. Jensen, K. Savolainen, S. Matikainen, H. Alenius, Long, needle-like carbon nanotubes and asbestos activate the NLRP3 inflammasome through a similar mechanism, ACS Nano 5 (2011) 6861–6870.

[15] H. Nagai, S. Toyokuni, Biopersistent fiber-induced inflammation and carcinogenesis: lessons learned from asbestos toward safety of fibrous nanomaterials, Arch. Biochem. Biophys. 502 (2010) 1–7.

[16] H. Haniu, Y. Matsuda, K. Takeuchi, Y.A. Kim, T. Hayashi, M. Endo, Proteomics-based safety evaluation of multi-walled carbon nanotubes, Toxicol. Appl. Pharmacol. 242 (2010) 256–262.

[17] M. Pacurari, X.J. Yin, J. Zhao, M. Ding, S.S. Leonard, D. Schwegler-Berry, B.S. Ducatman, D. Sbarra, M.D. Hoover, V. Castranova, V. Vallyathan, Raw single-wall carbon nanotubes induce oxidative stress and activate MAPKs, AP-1, NF-kappaB, and Akt in normal and malignant human mesothelial cells, Environ. Health Perspect. 116 (2008) 1211–1217.

[18] K. Pulskamp, S. Diabate, H.F. Krug, Carbon nanotubes show no sign of acute toxicity but induce intracellular reactive oxygen species in dependence on contaminants, Toxicol. Lett. 168 (2007) 58–74.

[19] V.E. Kagan, Y.Y. Tyurina, V.A. Tyurin, N.V. Konduru, A.I. Potapovich, A.N. Osipov, E.R. Kisin, D. Schwegler-Berry, R. Mercer, V. Castranova, A.A. Shvedova, Direct and indirect effects of single walled carbon nanotubes on RAW 264.7 macrophages: role of iron, Toxicol. Lett. 165 (2006) 88–100.

[20] C. Cheng, K.H. Muller, K.K. Koziol, J.N. Skepper, P.A. Midgley, M.E. Welland, A.E. Porter, Toxicity and imaging of multi-walled carbon nanotubes in human macrophage cells, Biomaterials 30 (2009) 4152–4160.

[21] R. Kato, K. Miyazawa, T. Nishimura, Z.M. Wang, High-resolution transmission electron microscopy of heat-treated C_{60} nanotubes, J. Phys: Conf. Ser. 159 (2009) 012024.

[22] K. Miyazawa, Synthesis and properties of fullerene nanowhiskers and fullerene nanotubes, J. Nanosci. Nanotechnol. 9 (2009) 41–50.

[23] K. Miyazawa, Y. Kuwasaki, A. Obayashi, M. Kuwabara, C_{60} nanowhiskers formed by the liquid–liquid interfacial precipitation method, J. Mater. Res. 17 (2002) 83–88.

[24] H. Nagai, Y. Okazaki, S.H. Chew, N. Misawa, Y. Yamashita, S. Akatsuka, T. Ishihara, K. Yamashita, Y. Yoshikawa, H. Yasui, L. Jiang, H. Ohara, T. Takahashi, G. Ichihara, K. Kostarelos, Y. Miyata, H. Shinohara, S. Toyokuni, Diameter and rigidity of multiwalled carbon nanotubes are critical factors in mesothelial injury and carcinogenesis, Proc. Natl. Acad. Sci. U.S.A. 108 (2011) E1330–E1338.

[25] P. Haberzettl, R. Duffin, U. Kramer, D. Hohr, R.P. Schins, P.J. Borm, C. Albrecht, Actin plays a crucial role in the phagocytosis and biological response to respirable quartz particles in macrophages, Arch. Toxicol. 81 (2007) 459–470.

[26] C. Dostert, V. Petrilli, B.R. Van, C. Steele, B.T. Mossman, J. Tschopp, Innate immune activation through Nalp3 inflammasome sensing of asbestos and silica, Science 320 (2008) 674–677.

[27] A. Rubartelli, Redox control of NLRP3 inflammasome activation in health and disease, J. Leukoc. Biol. 92 (2012) 951–958.

[28] M.T. Heneka, M.P. Kummer, A. Stutz, A. Delekate, S. Schwartz, A. Vieira-Saecker, A. Griep, D. Axt, A. Remus, T.C. Tzeng, E. Gelpi, A. Halle, M. Korte, E. Latz, D.T. Golenbock, NLRP3 is activated in Alzheimer's disease and contributes to pathology in APP/PS1 mice, Nature 493 (2013) 674–678.

Contents lists available at ScienceDirect

Journal of Crystal Growth

journal homepage: www.elsevier.com/locate/jcrysgro

Influence of the solution volume on the growth of C_{60} nanowhiskers

CrossMark

Kun'ichi Miyazawa [*], Chika Hirata, Takatsugu Wakahara

Fullerene Engineering Group, Materials Processing Unit, National Institute for Materials Science (NIMS), 1-1 Namiki, Tsukuba 305-0044, Ibaraki, Japan

ARTICLE INFO

ABSTRACT

The lengths and diameters of C_{60} nanowhiskers (C_{60}NWs) grown in solutions were investigated relative to the inner diameter of the glass bottle and the solution volume while maintaining the volumetric ratio of C_{60}-saturated toluene and isopropyl alcohol at 1:1. The mean lengths and diameters of the C_{60}NWs increased, and the distribution of the lengths and diameters broadened when increasing the solution volume. The mean crystal nucleus size of the C_{60}NWs was determined by analyzing the size dependence of C_{60}NWs on the solution volume. The lengths and diameters of C_{60}NWs asymptotically approach their upper limits when increasing the solution volume.

© 2014 Elsevier B.V. All rights reserved.

1. Introduction

Fullerene nanowhiskers (FNWs) are thin, needle-like crystals composed of fullerene molecules, such as C_{60}, C_{70}, $C_{60}[C(COOC_2H_5)_2]$, $Sc_3N@C_{80}$, and others [1–4]. The needle-like fullerene crystals with diameters below 1000 nm are known as fullerene nanowhiskers [2,3]. One-dimensional fullerene crystals are promising materials for optical, electrical and electronic devices, including superconductors [5–9], and controlling their size is essential. For example, the electrical resistivity of these materials decreases rapidly when decreasing the diameter of the C_{60}NWs [10,11]. The photoluminescence peak for the C_{60} microtubes shifts toward lower wavenumbers when decreasing their diameters [12]. Controlling the size of C_{60}NWs is also important during their mechanical applications because their Young's modulus changes relative to the diameter and aspect ratio (length/diameter) of the C_{60}NWs [13–15]. The growth of C_{60}NWs is influenced by the temperature, light, ratio of the poor solvent versus the good solvent for C_{60}, and concentration of water [16–19,22]. In our previous paper, the diameter of the C_{60}NWs was a linear function of the area of the liquid–liquid interface when the total volume of solvent is constant, while the inner diameter of glass bottle changes [20].

However, the length of the C_{60}NWs must also be controlled before any practical application. In the present paper, we will demonstrate how the length and diameter of C_{60}NWs change depending on the bottle size and the solution volume.

These analytical results will elucidate the synthesis of C_{60}NWs with size control.

2. Experimental

A C_{60}-saturated toluene solution was prepared by dissolving C_{60} powder (99.5% MTR Ltd.) in toluene (non-dehydrated, Wako Pure Chemical Industries, Ltd., Osaka, Japan); the undissolved C_{60} powder was removed via syringe filter with 450-nm pores (Puradisc TM, Whatman Inc., Clifton, USA).

The C_{60}NWs were synthesized through a modified LLIP method. Five different sizes of transparent glass bottles were used, as shown in Fig. 1. For the LLIP method, a C_{60}-saturated toluene solution was poured into a glass bottle and an equal amount of isopropyl alcohol (IPA) was layered onto the C_{60}-saturated toluene solution. The glass bottle was capped and manually mixed by shaking the bottle 30 times in order to obtain homogeneous precipitation of embryo C_{60} crystals [16]; afterwards, the bottles were stored in an incubator at 15 °C for 8 days to obtain well-grown C_{60}NWs, avoiding the destabilization of C_{60}NWs by the impurity water contained in the solvents [19]. The synthesis of C_{60}NWs was repeated three times for each size of glass bottle. Table 1 shows the amount of C_{60}-saturated toluene solution and IPA with the sizes of the glass bottles.

The lengths and diameters of the C_{60}NWs were measured via scanning electron microscopy (SEM) (FIB-SEM Hitachi NB5000). In the SEM observations, all the C_{60}NWs were collected from the above three glass bottles with the same size and put into a glass bottle containing IPA. After a gentle manual mixing for homogenization,

---

* Corresponding author. Tel.: +81 298604528; fax: +81 298604667.
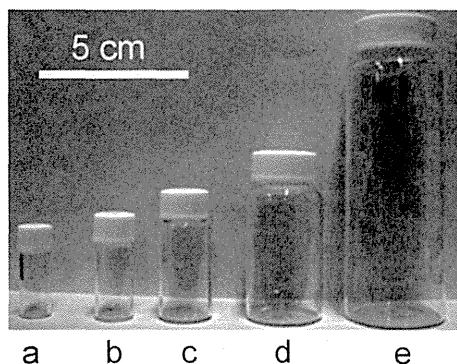 E-mail address: miyazawa.kunichi@nims.go.jp (K. Miyazawa).

Fig. 1. Transparent glass bottles with inner diameters of (a) 10 mm, (b) 12.5 mm, (c) 18 mm, (d) 27 mm and (e) 36.5 mm, respectively.

Table 1
Inner diameters of the glass bottles, and the amounts of C_{60}-saturated toluene solution and IPA used during the synthesis of the C_{60}NWs.

Glass bottles (Fig. 1)	Inner diameter (mm)	C_{60}-saturated toluene solution (cm^3)	IPA (cm^3)	Solution volume (cm^3)
(a)	10.0	0.75	0.75	1.5
(b)	12.5	1.5	1.5	3.0
(c)	18.0	4.0	4.0	8.0
(d)	27.0	10.0	10.0	20.0
(e)	36.5	40.0	40.0	80.0

parts of the C_{60}NWs in the glass bottle were sampled onto a Si substrate for SEM observations. One hundred C_{60}NWs were visualized to measure their lengths and diameters using randomly selected SEM images.

3. Results and discussion

As shown in Fig. 2, short and straight C_{60}NWs with uniform diameters along their growth axes were successfully synthesized in each glass bottle. In the SEM images, finer C_{60}NWs are observed when the bottle size decreases. Figs. 3 and 4 show that the distributions of the length and diameter for the C_{60}NWs broaden when increasing the bottle size.

The mean lengths and diameters of the C_{60}NWs are plotted relative to the inner diameters of the bottles, as shown in Figs. 5 and 6. The mean length and diameter increase linearly when increasing the inner diameter of the glass bottle. The standard deviations for the length and inner diameter of C_{60}NWs increase, reflecting the broader distributions observed with the larger bottle sizes. Therefore, the uniformity of the C_{60}NWs depends on the size of the glass bottle and diverges when increasing the size of the glass bottle.

In addition, the length and diameter decrease when decreasing the bottle size. The y-intercepts are the smallest mean size of C_{60}NWs, which can be treated as the nucleus for crystal growth; these particles should have a mean length of 2.1 μm and a mean diameter of 305 nm. The C_{60} nuclei should have a mean aspect ratio of 6.9 ($=2.1$ μm/305 nm).

However, the aspect ratio for each C_{60}NW was calculated using the same data shown in Figs. 5 and 6. As shown in Fig. 7, the aspect ratio is observed to increase and broaden when increasing the inner diameter of the bottle. Fig. 8 shows the relationship between the mean aspect ratio and the inner diameter of the bottle. The smallest aspect ratio can be determined by using the y-intercept in Fig. 8; this value is 10.8. However, this value does not coincide with the value above (6.9). The large discrepancy between 10.8
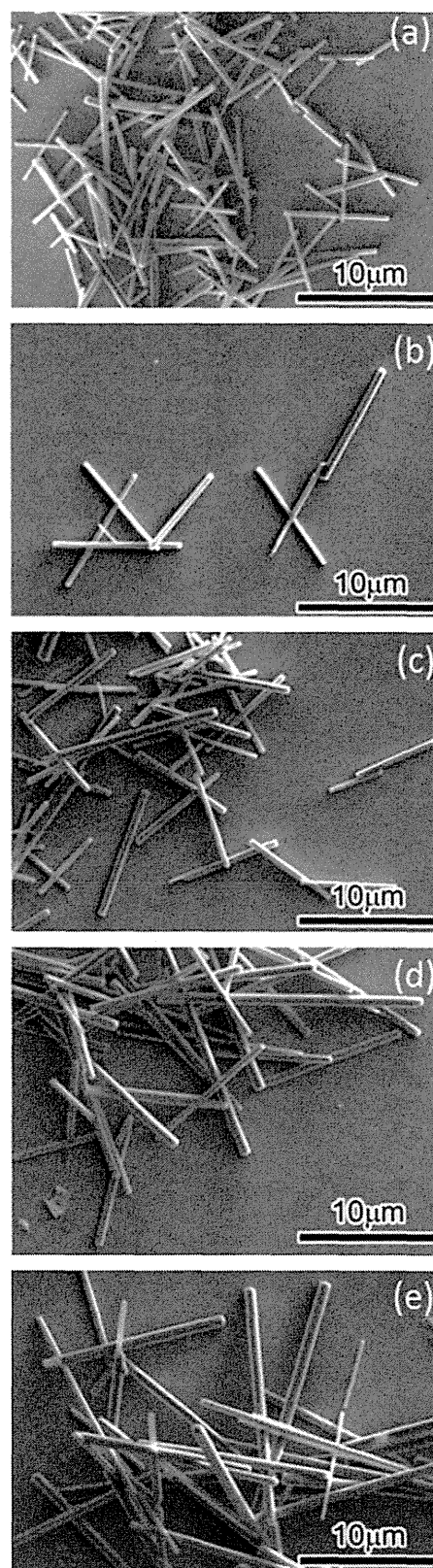

Fig. 2. SEM images of the C_{60}NWs synthesized using glass bottles with inner diameters of (a) 10 mm, (b) 12.5 mm, (c) 18 mm, (d) 27 mm and (e) 36.5 mm.

and 6.9 in the aspect ratios indicates that the sizes of the C_{60}NW nuclei were estimated incorrectly, suggesting that the curve fittings were performed incorrectly. This result should have arisen from the fact that the above curve fittings were performed only for